Extreme magnesium isotope fractionation at outcrop scale records the mechanism and rate at which reaction fronts advance

Philip A.E. Pogge von Strandmann[1,2*], Ralf Dohmen[2,3], Horst R. Marschall[2,4], John C. Schumacher[2], Tim Elliott[2]

[1]*Department of Earth Sciences, University College London and Department of Earth and Planetary Sciences, Birkbeck, University of London, Gower Street, London, WC1E 6BT*

[2]*Bristol Isotope Group, School of Earth Sciences, Bristol University, Wills Memorial Building, Queens Road, Bristol, BS8 1RJ, UK*

[3]*Institut für Geologie, Mineralogie und Geophysik, Ruhr-Universität Bochum, 44780 Bochum, Germany*

[4]*Department of Geology and Geophysics, Woods Hole Oceanographic Institute, Woods Hole, MA 02543, USA*

*Contact email: p.strandmann@ucl.ac.uk

Abstract

Isotopic fractionation of cationic species during diffusive transport provides novel means of constraining the style and timing of metamorphic transformations. Here we document a major (~1‰) decrease in the Mg isotopic composition of the reaction front of an exhumed contact between rocks of subducted crust and serpentinite, in the Syros mélange zone. This isotopic perturbation extends over a notable length-scale (~1 m), implicating diffusion of Mg through an intergranular fluid network over a period of ~100 kyr. These novel observations confirm models of diffusion-controlled growth of reaction zones formed between rocks of contrasting compositions, such as found at the slab-mantle interface in subduction zones. The results also demonstrate that diffusive processes can result in exotic stable isotope compositions of major elements with implications for mantle xenoliths and complex intrusions.

1.0 Introduction

Most of the Earth's crust and mantle are inaccessible to us. We therefore rely on natural exhumation to obtain samples from depth for the study of processes that operate more than a few kilometres below the surface. The tectonic return of subducted lithologies to the surface has been of considerable importance for constraining the sequence of prograde metamorphism at destructive plate margins. Elucidating these processes relies in large part on the correct interpretation of major and trace-element composition and isotopic signatures of the exhumed rocks. A subduction origin of some exhumed eclogites, for example, can be deduced from their stable isotopic signatures (e.g. anomalous $\delta^{18}O$ (Carmody et al., 2013; Desmons and O'Neil, 1978; Vogel and Garlick, 1970)) of these high temperature mineral assemblages, that were likely generated at much lower temperatures near the surface. More recently, however, it has emerged that the stable isotope ratios of some elements, such as Li, may also be strongly perturbed by diffusive processes operating at high temperatures (Jeffcoate et al., 2007; Richter et al., 2003; Rudnick and Ionov, 2007; Teng et al., 2006), without invoking prior near-surface interactions (Elliott et al., 2004). The slab-mantle interface is particularly prone to diffusion processes, because of the juxtaposition of ultramafic mantle rocks with metasediments and metabasaltic rocks that show strong chemical contrasts for most chemical components (Bebout, 2012; Marschall and Schumacher, 2012; Penniston-Dorland et al., 2012; Penniston-Dorland et al., 2010; Sorensen and Barton, 1987). Here we further assess the potential of such diffusive transport to perturb isotopic signatures by making a detailed study across an exhumed crust-mantle contact using the major element magnesium. In addition, we demonstrate how length scale and shape of measured

diffusion profiles can be used to extract information on the mechanisms and timescales involved in the growth of reaction zones.

Bulk diffusion can occur on many different scales within silicate rocks (Watson, 1991; Watson and Baxter, 2007). Major elements, such as Mg and Fe, have repeatedly been shown to diffusively exchange in silicate minerals (interdiffusion) (Chakraborty, 1997), and Mg may also diffuse on larger scales in bulk rock processes (Miller et al., 2009; Sanford, 1982). However, advective metasomatism must also be considered as an additional operating mechanism, and some geochemical studies on reaction zone rocks have altogether neglected the effects of diffusion and interpreted their formation as solely controlled by advection with far-reaching consequences for their geochemical interpretation (Breeding et al., 2004).

Experimental and natural studies have shown that the diffusion of species along a chemical potential gradient can be accompanied by isotopic fractionation, because the lighter isotopes will diffuse faster than the heavier ones (Richter et al., 2003). Of all the major elements, Mg isotopes are ideally suited to reveal the effects of diffusion, because of their large relative mass differences and commonly occurring strong chemical potential gradients in nature. Experiments have demonstrated Mg isotope fractionations as great as 8‰ by chemical diffusion (Richter et al., 2008). Natural rock studies have shown fractionations on mm-scales between juxtaposed felsic and mafic rocks (Chopra et al., 2012; Teng et al., 2011), and inferred it during diffusive replacement of H^+ during xenolith degassing (Pogge von Strandmann et al., 2011), and Mg-Fe interdiffusion in olivine (Dauphas et al., 2010). Therefore diffusion of major elements is a significant process during metamorphism and metasomatism, not only because it determines changes in mineral assemblages from thin section to

outcrop scale, but also because it has the potential to significantly alter stable isotope ratios of minerals and rocks.

2.0 Field area and sample petrography

The island of Syros displays a sequence of rocks of the lower unit of the Attic-Cycladic Crystalline Complex (Dürr et al., 1978). The major part of the island is composed of interlayered pelitic schists and marbles dipping north to NE (Hecht, 1984; Keiter et al., 2011). The north-eastern part of the island comprises a mélange zone of composed of metagabbros, eclogites, glaucophane schists, meta-plagiogranites, serpentinites and metasediments embedded in a chlorite-rich mafic-ultramafic matrix. It mainly preserved a blueschist- to eclogite-facies metamorphic overprint along with many well-exposed contacts between contrasting lithologies that are characterised by the formation of reaction zones, also called *blackwalls* (Brocker and Enders, 2001; Marschall et al., 2006; Okrusch and Brocker, 1990; Ridley, 1984; Seck et al., 1996). Metamorphic peak conditions were estimated at 470−520 ℃ and 1.3−2.1 GPa by different authors for different rock types (Keiter et al., 2004; Okrusch and Brocker, 1990; Rosenbaum et al., 2002; Trotet et al., 2001). The *P–T* conditions reported for the formation of Syros blackwalls by Breeding et al. (2004) [1.17–1.23 GPa, 500–550 °C], Marschall et al. (2006) [0.62–0.72 GPa, 400–430 °C] and Miller et al. (2009) [1.2 GPa, 430 ℃] show that the northern Syros mélange was exhumed from depths of about 55–75 km and underwent incursion of hydrous fluids at shallower levels of 25–35 km. One detailed suite of samples was collected from the northern extreme of Lía Beach on the north-western side of Syros (N37°29.419′ E024°54.089′; elevation of 8 m above sea level). The sequence represents a continuous exposure of a

1–2 m thick reaction zone located between meta-volcano-sedimentary schists and a large (∼50 m), continuous lens of serpentinite (Fig.1, 2; Miller et al., 2009). We have analysed a profile of 16 well-characterised whole-rock samples from a reaction zone formed at blueschist-facies conditions, at the contact of serpentinite and meta-volcaniclastic rock (garnet-phengite-epidote-glaucophane schist) within the high-pressure mélange zone of Syros, Greece (Miller et al., 2009). Samples were removed using a diamond-tipped rock saw to obtain three continuous sections of samples that together cover a complete section across the reaction zone (Miller et al., 2009). The individual samples were taken from ~2 cm wide slabs cut perpendicular to the sections, i.e. slabs oriented parallel to the initial lithologic contact. The distance from the contact given for each sample depicts the distance of the centre of the 2 cm slab to the initial contact. Both contacts (upper and basal) are still intact and accessible in the outcrop. However, no single complete section from the schist into the serpentinite could be sampled, so that the complete profile had to be reconstructed from three overlapping sections that were taken within a distance of a few meters (Fig. 1). Reconstruction of the relative positions of the three sections was achieved based on field relations and petrography. The reaction zone has been sub-divided into the following five zones, based on their mineralogical compositions (Miller et al., 2009): Zone I (unaltered meta-volcaniclastic rock), Zone II (glaucophane+chlorite+epidote), Zone III (omphacite+epidote+chlorite), Zone IV (chlorite schist), and Zone V (serpentinite) (Fig. 2, 3, Table 1)[1]. The distances for individual samples listed by Miller et al. (2009) are simple measurements along the sampled profiles. In this study, we adjusted these distances to represent the distance of

---

[1] Note that some zones were mislabelled in Tables 1 and 3 of Miller et al. (2009), whereas they are correctly described and labelled in their text and figures. The correct zones are also given in Fig. 2.

each sample from the initial garnet-glaucophane schist to the serpentinite contact. This, of course, does not change the relative distances between samples within the profiles, which were correctly listed in Table 1 of Miller et al. (2009).

Zone I represents the meta-volcaniclastic rock (originally basaltic to intermediate tuffs) consisting of glaucophane (Gln)+epidote (Ep)+phengite (Ph)+garnet (Grt) with accessory rutile (Rt) and ilmenite (Ilm). Quartz is present as inclusion in garnet (Grt). Chlorite (Chl) is restricted to halos replacing Grt in samples further away from the reaction zone (Fig. 4a,b). Samples in closer vicinity to the reaction zone show a more advanced replacement of Grt by Chl and Ph, which is interpreted as the increasing influence of the mineral replacement of the reaction zone (Fig. 4b, c). In those samples, Chl also appears in the Gln+Ep matrix of rocks (Fig. 4c).

Zone II represents the reaction zone in contact with the Zone-I schist. It consists of Gln+Ep+Omp and minor albite (Ab) and tourmaline (Tur). Rutile is replaced by titanite (Ttn). No Grt is present, but pseudomorphs of Chl+Gln+Ep after Grt have approximately the same abundance as Grt has in Zone-I rocks (Fig. 4d).

Zone III is defined by the occurrence of omphacite (Omp), while Gln is absent or restricted to pseudomorphs after Grt (Fig. 4e-h). The assemblage present in all samples from this zone is Omp+Chl+Ep with minor Ab and Ttn. Pseudomorphs after Grt are present and show a similar abundance to Zone II (Fig. 4e,g). The abundance of Chl in the samples increases continuously through Zone III towards the serpentinite (Fig. 4e-h). Samples closer to Zone IV show only minor or no Omp and Ab and lower abundances of Ep. The transition from Zone III to Zone IV is characterised by the disappearance of Ep (Fig. 4h).

Zone IV is the zone that is in contact with the serpentinite and consists of chlorite schist. Gln and Omp are absent from this zone, and no pseudomorphs after Grt could

be identified with any certainty (Fig. 4h-n). Chl is darker green and more Fe rich in vicinity to Zone III, but is continuously paler and more Mg rich as the contact to the serpentinite is approached (Fig. 43h-n). The chlorite schist contains Ttn at the contact with Zone III (Fig. 4h-k). In its central part the Ti phase is Rt (Fig. 4i-m), while in contact to the serpentinite, an opaque phase is present (Fig. 4m,n).

Zone V represents the serpentinite, which consists of antigorite intergrown with small magnetite grains and larger (mm-sized) chromite grains (Fig. 4o,p). Some samples show an undeformed mesh texture of antigorite and magnetite (Fig. 4p), which is typical for undeformed serpentinised peridotite. Veins in the serpentinite (Fig. 4o,p) contain some Tlc and Chl, but are dominated by Atg. Talc and Chl occur only in close vicinity to the reaction zone. Samples taken at larger distances from the contact consist of antigorite+magnetite.

This type of reaction zone represents interaction of crustal and mantle components at high pressures, and is considered an analogue for processes occurring at the slab-mantle interface (Marschall and Schumacher, 2012; Miller et al., 2009). The metamorphic relationships in the Syros mélange are complex, occur at relatively low temperatures (~430°C, ~1.2GPa), and are thought to reflect two dominant processes (Miller et al., 2009): diffusion of chemical components (e.g. Mg, Cr, Ni) perpendicular to the contact driven by activity contrasts between the juxtaposed rocks (i.e. across the slab-mantle boundary). The metamorphic reactions led to increased porosity in the chlorite-rich zone, which in turn allowed porous flow parallel to the contact, which leached and transported fluid mobile elements (e.g. LILE and Si). Fluid immobile elements (e.g. Al, Ti, Y and Zr) have demonstrably maintained their initial abundances, whilst elements such as Ca, Sr and the LREE are concentrated due to the stabilisation of Ca-minerals and monazite at intermediate points in the reaction

zone (Miller et al., 2009). This behaviour highlights the different, and partially unrelated, behaviour exhibited by different elements in a single profile, due to differing elemental properties, and the changing chemical gradients caused by the stabilisation of different minerals.

Petrographic evidence from the thin sections show that Zones II, III and IV sequentially replace the initial assemblage of Zone I. Reaction zone growth is initiated by an influx of MgO into the metavolcanic rock right at the serpentinite contact, which produced a very thin replacement sequence similar to the assemblages found in the mature Zones II, III and IV: a layer of chlorite at the serpentinite contact, followed by Omp+Chl+Ep (=Zone III assemblage) and Gln+Chl+Ep (=Zone II assemblage). These zones grew as more MgO entered from the serpentinite, but at the same time the earlier-formed Zone-II assemblage would be replaced by a Zone-III assemblage and the Zone-III assemblage by Zone-IV chlorite, as all three zones grow wider and replace unaltered metavolcanics garnet-glaucophane schist of Zone I.

3.0 Methods

Whole-rock major and trace element concentrations were determined on powdered samples by X-Ray fluorescence, with data reported in Table 2.

Mg isotope ratios were analysed on the same powders. The purification and analytical methods are well-described elsewhere (Pogge von Strandmann et al., 2011; Pogge von Strandmann et al., 2012), but briefly, samples were purified using a 2-stage cation exchange chemistry (AG50W X-12), with 2.0M HNO_3 as an eluent. Mineral separates were analysed by the same method, except where the Ti/Mg ratio was very high, in which case an additional column using TRU-Spec resin was applied to quantitatively remove Ti (Pogge von Strandmann et al., 2012). Samples were

analysed on a Thermo Finnigan Neptune multi-collector inductively coupled mass spectrometer (MC-ICP-MS), with an Elemental Scientific Inc. Apex-Q introduction system. Measurements were bracketed by the standard DSM-3 (Galy et al., 2003), and are reported as the ‰ deviation from that standard. Analytical reproducibility on $\delta^{26}Mg$ is ±0.06‰, as shown by repeated analyses of several different international rock standards (Pogge von Strandmann et al., 2011).

For O isotope analyses, whole-rock sample powders were pressed into pellets using a Quick KBr pellet press, and analysed by ILFT (CO_2 laser) by Dr. Zhengwrong Wang at Yale University using methods described previously (Eiler et al., 1996; Wang et al., 2011). Three repeats were analysed of each sample, and results are listed in Table 2. The 2 standard deviations for the three repeats varied between 0.04 and 0.24 ‰ for the set of samples investigated here.

4.0 Results

The ~10.5 m profile includes an MgO decrease of over a factor of 5, from ~37 to ~7 wt%, concentrated in ~0.5 m across the contact of the serpentinite to the meta-volcanic schist (Fig. 5). Other elements also exhibit diverse behaviour related to a number of processes: diffusion due to individual chemical activity gradients, leaching by fluid flow, or concentration due to mineral growth (Miller et al., 2009).

Both the serpentinite and the unaltered schist sampled at distance from the contact have Mg isotope ratios similar to that of the bulk silicate Earth ($\delta^{26}Mg$ ~ -0.21‰ (Bourdon et al., 2010; Handler et al., 2009; Pogge von Strandmann et al., 2011; Teng et al., 2010)). The chlorite-rich zone on the crustal side of the contact (reaction zone IV), however, contains significantly lighter Mg isotope ratios ($\delta^{26}Mg$ ~ -1‰; Table 2), concentrated within ~20cm of the profile. Zone III contains $\delta^{26}Mg$

values intermediate between the anomalously light ratios of Zone IV, and the "pristine" ratios of Zones I and II (Fig. 5).

Equally, the unaltered rocks at distance from the contact show very similar $\delta^{18}O$ values of $+5.4 \pm 0.1$ ‰ for the glaucophane schist and $+5.5 \pm 0.2$ ‰ for the serpentinite (Table 2). A slight decrease is observed in $\delta^{18}O$ throughout Zones II to IV to the initial contact, where the chlorite schist has a value of $+4.97 \pm 0.08$ ‰ (Fig. 6). A negative excursion to the smooth decrease is found in Zone III, which shows values of approximately $+4.5$ ‰. In contrast, $\delta^{18}O$ values in the serpentinite increase towards the lithologic contact and are highest ($+6.0 \pm 0.2$ ‰) where the serpentinite is in contact to the chlorite schist of Zone IV (Fig. 6).

The $\delta^{18}O$ values of hydrous fluids in equilibrium with each individual sample throughout the profile were also calculated in order to evaluate the O isotope profile independent of the changes in the modal compositions of the rocks. The calculation is based on the modal composition of the rocks and temperature-dependent mineral-fluid fractionation factors, taking into account the mineral compositions and calculating fractionation in solid solutions from endmembers (Zheng, 1991, 1993a, b, 1996). The values were calculated for $T = 430^{\circ}C$, which is the temperature of formation of the reaction zone (Miller et al., 2009). The calculated fluid shows a high value in Zones I and II and in Zone V in samples close to the contact. Zone V samples at a larger distance to the contact would be in equilibrium with fluids of lower $\delta^{18}O$ values. Zone-III and IV fluids show lower $\delta^{18}O$ values by ~0.7‰ compared to Zones II and V in contact to them (Fig. 6). One sample shows an additional ~0.5‰ negative excursion.

Some similarities exist between the shape of the Mg isotope profile and the calculated fluid $\delta^{18}O$ profile, but this is contrasted by significant differences between

the two. Both profiles show low values in Zones III and IV and an increase in Zone V towards the contact. Yet, the drop from high to low in the O isotope profile occurs on the serpentinite side of the contact, while the drop from high to low in the Mg isotope profile occurs within the chlorite schist. The lowest δ^{26}Mg values are found in Zone IV, while δ^{18}O of Zone III are equally low as in Zone IV. Overall, there is no correlation between the δ^{26}Mg and the δ^{18}O compositions (Fig. 7).

5.0 Discussion

5.1 Mg and O isotope fractionation mechanisms

A theoretical possibility is that the reaction zone could have formed at the seafloor prior to subduction. Chlorite-talc rich reaction zones and Ca-rich alteration products (rodingites) have been described from the seafloor, where they occur at the contact between mafic (gabbro) and ultramafic (serpentinite) rocks (Bach et al., 2013). If the observed chemical and mineralogical succession formed prior to subduction, this would mean that the observed isotope anomalies would have to be ascribed to that same pre-subduction process. However, the reaction zone has equilibrated under high-pressure metamorphic conditions, as is evident from the mineral assemblages. Also, replacement of garnet and glaucophane by chlorite and phengite shows that at least part of the metasomatic activity must have occurred after the rocks had reached their peak metamorphic P-T conditions. Metasomatic activity at conditions of 430 °C and 1.2 GPa is evident from the recrystallised assemblage. Large, metasomatic tourmaline intergrown with omphacite and other high-P blackwall minerals are further evidence for the high-pressure metasomatic activity. No evidence can be presented to disprove the possibility that some of the chemical exchange between serpentinite and metavolcanics rocks already occurred prior to subduction.

However, we consider this unlikely for the following reasons: the unaltered, mantle-like $\delta^{18}O$ value of the serpentinite argues against seafloor serpentinisation, as seafloor alteration typically leads to a strong decrease or increase of $\delta^{18}O$ (depending on temperature) and to the formation of large talc or rodingite zones (Bach et al., 2013). In addition, the preserved mesh texture in the serpentinite shows that the ultramafic rock was not subjected to penetrative deformation after serpentinisation of the peridotite precursor, and hence argues for a relatively late stage of serpentinisation. A possible source of peridotite in the Syros mélange sequence is the mantle wedge above the subducting slab (Marschall and Schumacher, 2012; Miller et al., 2009). This interpretation would suggest that the metavolcanic rock and the peridotite were tectonically juxtaposed possibly at peak pressure conditions (2.0 GPa), followed by serpentinisation of the peridotite and mutual exhumation of the two rock types in the mélange. Large parts of the blackwall formed during exhumation during a stage of more intense fluid flux, or at least fluid presence, that may have lasted for ~100 kyr.

There are therefore three possible well-established mechanisms to explain the formation of the very light isotope ratios observed in the reaction zone under high-P conditions: 1) equilibrium fractionation by one or more of the minerals present, which affects the bulk rock isotope composition; 2) the reaction zones (Zones III & IV) equilibrated with an isotopically light fluid and reflect advective fluid flow parallel to the lithologic contact; 3) kinetic isotope fractionation due to diffusive transport of magnesium through the polycrystalline reaction zone perpendicular to the lithologic contact.

Explanation #1 is ostensibly supported by the correlation of the bulk rock $\delta^{26}Mg$ with the modal abundance of chlorite (Fig. 8a), potentially suggesting that chlorite would favour light Mg isotopes during equilibrium fractionation from a

buffered fluid composition. However, mass balance would then require that other

minerals or fluids be highly enriched in heavy Mg isotopes, given that chlorite

dominates the MgO budget in the reaction zone (Fig. 8b). Mineral-separate analyses

of the analysed rocks in this profile show that the other significant Mg hosts in these

rocks (omphacite, glaucophane, tourmaline) do not have δ^{26}Mg values significantly

different from chlorite (Fig. 9, Table 3). Isotopically light garnets could also not cause

low bulk rock δ^{26}Mg patterns, because the Mg concentration and modal abundance of

garnet was never high enough to dominate the whole-rock compositions. Equilibrium

fractionation between a percolating fluid and the bulk rock is equally unlikely as a

cause for the low δ^{26}Mg values, given that fluid-solid reactions tend to result in an

isotopically heavy solid (Tipper et al., 2006). Further, some high chlorite samples

have relatively high δ^{26}Mg (Fig. 8), which is also better explained by the diffusion

processes described below.

Explanation #2, equilibration of the reaction zone with a fluid with low δ^{26}Mg,

would have affected the zones with lower MgO concentrations (Zones II + III) more

than MgO-rich Zone IV. Yet these zones have higher δ^{26}Mg than Zone IV despite

their lower MgO content. This could only be reconciled assuming a strong gradient in

contact-parallel fluid flux from very high fluid/rock ratios in large parts of Zone IV to

low fluid/rock ratios in Zones II and III. However, δ^{26}Mg values are very

heterogeneous throughout Zone IV, but they vary systematically as a function of

distance from the contact. They do not show a constant value as would be expected

from complete equilibration of this zone with an external fluid. In fact, the sample

closest to the contact has a higher δ^{26}Mg value than the initial value. In addition, in

order to explain the O isotope patterns, this fluid would also have had to have low

δ^{18}O values. Yet, low δ^{26}Mg and low δ^{18}O are observed in different zones,

respectively. Zones III and IV would have to be in equilibrium with a fluid with a

$\delta^{18}O$ of ~ +3.8‰ (with one lower outlier at ~ +3.2 ‰). Zones III and IV were

apparently both affected by enough fluid flow to completely equilibrate the whole

rocks with the fluid for oxygen isotopes. However, note that Mg isotopes in Zone III

are not as low as in Zone IV, despite its much lower MgO abundance, which should

have facilitated the isotopic overprint. Also, in this model, a second, high-$\delta^{18}O$ -high-

$\delta^{26}Mg$ fluid would be required to explain the isotopically heavy signatures in Zone V

in the vicinity of the contact. The combined $\delta^{18}O$ and $\delta^{26}Mg$ data hence show that the

reaction zone cannot have interacted with a single isotopically light fluid,

demonstrating that the light Mg isotopes were not caused by any straight-forward

scenario of advective contact-parallel fluid flow.

Explanation #3, isotope fractionation induced by diffusion, seems to be

plausible since strong chemical gradients were present and the phase assemblage in

the different zones can be explained by a continuous change in the chemical potentials

of MgO and CaO throughout the mélange zone (Miller et al., 2009). However, the

continuous decrease (with discontinuity between zone III and IV) in Mg through the

reaction zone cannot be explained solely by solid-state diffusion through the silicate

lattice (type-A regime (Harrison, 1961)), because metamorphic temperatures were far

too low (~430°C) for this process to occur over the observed length scales. Grain

boundary diffusion or fluid diffusion may be more efficient, but, finally, the Mg

isotopes fractionated by this method have to somehow enter the solid phase. In

addition, diffusion modelling indicates that for diffusive fractionation the largest

anomaly coincides with the point of strongest concentration gradient in the

concentration profile (Gallagher and Elliott, 2009). In the case of this study, however,

this behaviour cannot explain the approximately homogeneous $\delta^{26}Mg$ distribution in

the chlorite zone (Zone IV), because the complexity of the various zones requires that their growth rates need to be taken into account.

The hypothesis that diffusion must in some way be responsible for the Mg isotope anomaly and the growth of the reaction zone is also validated by the O isotopes, which suggest that light O was transported from the serpentinite into the reaction zone. This process decreased $\delta^{18}O$ of the chlorite schist and elevated the value of the serpentinite close to the contact (Fig. 6). This light O signature of the fluid may have been caused by equilibrium fractionation between minerals and fluids, or by kinetic fractionation due to faster diffusion of ^{16}O-rich species compared to ^{18}O-rich species, or by a combination of both. However, it is clear that low O and Mg isotope values do not exist in the same part of the profile (Fig. 7), and hence explaining the observed isotope patterns in the reaction zone by contact-parallel fluid flux would require at least three different fluids: a high-$\delta^{18}O$-high-$\delta^{26}Mg$ in Zone V, a low-$\delta^{18}O$ -low- $\delta^{26}Mg$ in Zone IV and a low-$\delta^{18}O$ -moderate-$\delta^{26}Mg$ fluid in Zone III. Yet, even this complex scenario would not explain the outliers at the contacts between Zones III and IV and IV and V, or indeed the trace element variability observed by Miller et al., 2009. Figure 7 therefore demonstrates that no single fluid composition can be identified that would explain the path through the O-Mg isotope space by advective contact-parallel fluid flow. Hence, these alterations cannot be explained by different degrees of equilibration with the same external fluid composition. Diffusive isotope fractionation is, therefore, the most likely cause of the observed Mg isotope patterns. This process is discussed and modelled in the following sections.

5.2 Background from the literature on metasomatic reaction zones

The metasomatic reaction zone at the contact of the serpentinite and glaucophane
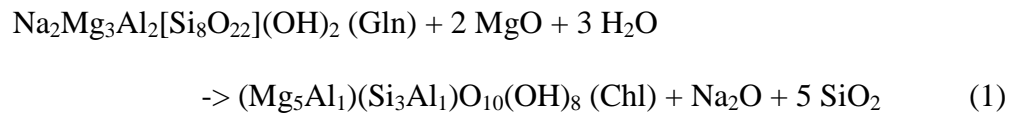
schist has a layered structure with three different zones (Zones II, III and IV), where

significant changes in mineralogy occur as described above, and in Miller et al.

(2009). Such a layered structure is characteristic for a diffusion-controlled reaction

zone of which numerous similar examples can be found in the literature (e.g.

(Fukuyama et al., 2006)). The formation of the intermediate layers is driven by the

strong chemical gradient between the serpentinite and the glaucophane schist. Once a

layer is formed that separates the two lithologies, the continuous growth of layers

requires the diffusive transport of elements. Diffusion-controlled reaction layers have

been extensively discussed in several classical papers (Fisher, 1973; Joesten, 1977).

These studies applied the methods of irreversible thermodynamics to explain the

detailed sequence of layers and interpreted them in terms of the relative mobility of

the oxide components. Recent experimental studies on the kinetics of multi-layer

formation also unequivocally document that the formation of these layers is diffusion

controlled (Gardes and Heinrich, 2011; Gardes et al., 2011). Furthermore, the

direction of growth of the individual layers can be variable, depending on the mobility

of the different components. Hence, a layer may grow only at either one end of the

layer or at both (see for example the discussion for the reaction Fo + Qtz = En (Abart

et al., 2004; Abart et al., 2009)). In general, the whole process is considered a multi-

component diffusion process, where gradients of the chemical potentials of the oxide

components drive the mass flux. Even in cases where the diffusing species are not

oxide components (e.g., in an aqueous fluid), thermodynamic treatment of these

processes allow to describe the fluxes with Onsager coefficients of the oxide

components. These coefficients are directly related to the mobility and the diffusion

coefficients of the components (e.g. Fisher, 1973). For the present case it was shown

by Miller et al. (2009) that the mineralogical sequence found within the reaction zone

can be explained at isobaric, isothermal conditions by continuously varying the chemical potential of MgO and CaO (at T = 430 °C and P = 1.2 GPa) and therefore the individual reaction zones (or each point across the zone on a thin section scale) reflect local equilibrium. However, it should be noted that this does not necessarily imply that MgO and CaO are mobile components in this reaction zone. An additional complexity here compared to the cases discussed in the classical papers is that the reaction zone is apparently an open system as is indicated by the enrichment of fluid-mobile elements, such as Li and B and depletion of LILE and Si. There are new models available that consider open system fluxes in reaction zones (e.g., (Ashworth and Birdi, 1990)). However, the aim of this paper is not to decipher the kinetics of the reaction zone in all detail. Instead, it focuses on its implications for the fractionation of stable isotopes. We, therefore, give a simplified scenario for the formation of Zones II–IV in which isotope fractionation is observed.
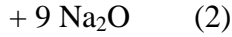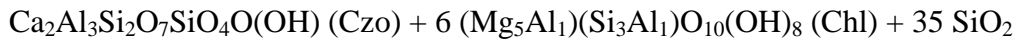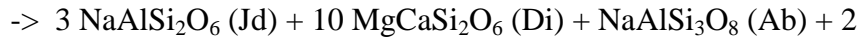
5.3 Reaction mechanisms

As mentioned above there are in principle various possibilities for the individual reactions occurring at the layer interfaces, which determines the direction of the layer growth. The reactions at the interfaces in turn are coupled to the relative mobility of the oxide components. Here we assume that MgO, CaO, Na_2O and H_2O are the more mobile components across the reaction zone and in addition assume that the chemical potential of SiO_2 and maybe other components such as K_2O are buffered or at least affected by the fluid in this partially open system. The concentrations of the components Al_2O_3, TiO_2 and ZrO_2, which are generally considered to be immobile components in fluid-bearing systems, show relatively constant abundances throughout zones I to IV and a sharp decrease in abundances between zones IV and V (Miller et
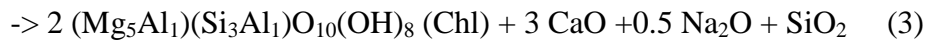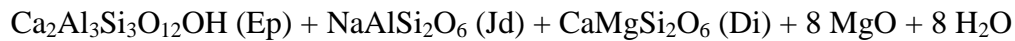
al., 2009). We therefore assume that the initial contact was located at the interface between zones IV and V (Fig. 10). Zones I and IV contain rutile, while titanite replaced rutile within zones II and III, formed by the reaction of rutile with excess SiO_2 and CaO delivered from other reactions as will be discussed below. Therefore, the growth of the reaction zones mainly occurred from the initial contact between zones IV and V into the glaucophane schist and elements required to form the new phase were mainly transported from the serpentinite into the reaction zone. The most prominent features of the reaction zone are: (i) the mode of chlorite increases towards the serpentinite, with zone IV consisting almost exclusively of chlorite (plus residual rutile and other accessory minerals) (ii) The stability of omphacite within zone III. Starting at zone II where chlorite is apparently formed at the expense of glaucophane, a possible endmember reaction leading to the formation of chlorite (clinochlore) by transferring MgO from the serpentinite into this zone could be (see Fig. 4c–f):

$$Na_2Mg_3Al_2[Si_8O_{22}](OH)_2 \text{ (Gln)} + 2 \text{ MgO} + 3 \text{ H}_2O$$

$$\rightarrow (Mg_5Al_1)(Si_3Al_1)O_{10}(OH)_8 \text{ (Chl)} + Na_2O + 5 \text{ SiO}_2 \qquad (1)$$

According to this reaction Na_2O and SiO_2 are liberated. Whereas the latter can be leached from the reaction zone due to the fluid flow parallel to the contact as is indicated from the depletion of SiO_2 in the bulk rocks, the former may be redistributed within the zone into other phases, mainly tourmaline, omphacite and albite. At the transition from zone II to zone III omphacite becomes stable and glaucophane is almost completely consumed. A plausible reaction describing this process is (Fig. 4d–f):

11 $Na_2Mg_3Al_2[Si_8O_{22}](OH)_2$ (Gln) + 7 MgO + 14 H_2O + 14 CaO

-> 3 $NaAlSi_2O_6$ (Jd) + 10 $MgCaSi_2O_6$ (Di) + $NaAlSi_3O_8$ (Ab) + 2

$Ca_2Al_3Si_2O_7SiO_4O(OH)$ (Czo) + 6 $(Mg_5Al_1)(Si_3Al_1)O_{10}(OH)_8$ (Chl) + 35 SiO_2

+ 9 Na_2O (2)

The chemical potential of MgO increases towards the serpentinite as well as the total
flux of MgO. This is clearly demonstrated by calculations of the chemical potential of
MgO at 430°C and 1.2 GPa using the Perple_X application suite (Fig. 10d)(Connolly,
2005, 2009), providing an obvious indication of the chemical driving force of Mg
diffusion. Consequently more chlorite is produced by reaction 1 within zone III.
Finally, at the interface of zone III and IV omphacite and epidote become unstable to
form chlorite. The reaction is then (Fig. 4g–h):

$Ca_2Al_3Si_3O_{12}OH$ (Ep) + $NaAlSi_2O_6$ (Jd) + $CaMgSi_2O_6$ (Di) + 8 MgO + 8 H_2O

-> 2 $(Mg_5Al_1)(Si_3Al_1)O_{10}(OH)_8$ (Chl) + 3 CaO +0.5 Na_2O + SiO_2 (3)

The latter reaction implies that in addition to SiO_2, Na_2O was also lost from the
reaction zone via the fluid flow, which is in agreement with the whole-rock analyses,
and is also shown by the chemical potentials of these species (Fig. 10d). Assuming
Al_2O_3 is immobile (Miller et al., 2009), the relatively smooth changes in MgO, CaO
and SiO_2, relative to the step-change shown by Al_2O_3, suggests that in order to
achieve equilibrium between the chlorite schist and the serpentinite, silica and lime
must have been leached, and magnesia added. In this model, the serpentinite would
act as an infinite reservoir for H_2O and MgO where the flux of these components is

controlled by the breakdown of serpentinite according to the following reaction (Fig. 4o–p):

$$2\ Mg_3Si_2O_5(OH)_4\ (Atg) \rightarrow Mg_3Si_4O_{10}(OH)_2\ (Tlc) + 3\ MgO + 3\ H_2O \qquad (4)$$
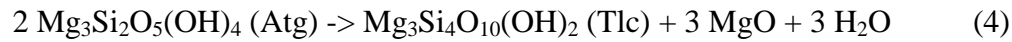
Alternatively, because SiO_2 is a very fluid mobile component, talc within zone V could have formed by reaction of aqueous SiO_2 with serpentine:

$$Mg_3Si_2O_5(OH)_4\ (Atg) + 2\ SiO_2 \rightarrow Mg_3Si_4O_{10}(OH)_2\ (Tlc) + H_2O \qquad (5)$$

Alternatively, chlorite in zone IV could have formed by the breakdown of serpentine according to the following reaction:

$$2\ Mg_3Si_2O_5(OH)_4\ (Atg) + Al_2O_3 \rightarrow (Mg_5Al_1)(Si_3Al_1)O_{10}(OH)_8\ (Chl) + MgO + SiO_2 \qquad (6)$$
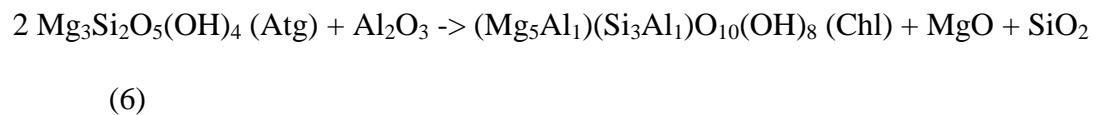
However this would require an influx of Al_2O_3, and this would also imply that chlorite in zone IV had grown into the serpentinite zone, which is inconsistent with the immobile element pattern across the reaction zone.

So far we have only considered the flux of components through the intergranular fluid, implicitly assuming an interconnected fluid network in the rock. In the next section we give arguments that other diffusion pathways in the rock can be ignored as they are insignificant.

5.4 Diffusion pathways and efficiency

Within the reaction layers, which consist of a polycrystalline and multi-phase material, there are various different diffusion pathways available (e.g., Watson and Baxter 2007; Dohmen and Milke 2010). For the present purpose we can broadly classify them into three types: lattice diffusion (i.e., diffusion within the grain interiors), grain boundary diffusion (i.e., diffusion along mineral-mineral contacts), and fluid diffusion (i.e., diffusion along water-rich fluid present in grain edges and pores). We assume that the fluid is interconnected and forms a network for diffusive transport through the bulk rocks (Watson, 1991). Here we discuss the potentially most efficient diffusion pathway and estimate a diffusion coefficient for Mg.

Diffusion within the grain boundaries and through the fluid can be generally considered as many orders of magnitude faster than lattice diffusion (e.g. Watson and Baxter 2007). For the present system we have to consider a very low temperature (~430 °C; Miller et al., 2009) at which diffusion within the lattice is usually extremely sluggish. Experimental data for diffusion of the relevant elements, e.g., Mg, O, Si, etc. are rare for the minerals of interest but we give a few numerical examples here to illustrate the insignificance of diffusive transport through the mineral grains. For example, the tracer diffusion coefficient of Mg for pure diopside (Zhang et al., 2010) can be used as an estimate for the omphacite, from which we obtain $D_l = 3.1 \times 10^{-27}$ m^2/s at 400 °C. To our knowledge there are no relevant diffusion data available for chlorite, epidote, antigorite, talc, and tourmaline. Just to consider another value, we have calculated D_l of Sr in albite from the Arrhenius relationship (Cherniak, 1996), which gives 1.19×10^{-26} m^2/s at 400 °C. From these two numbers we can infer that even after 100,000 years the diffusion penetration distance of Mg within the minerals is on the order of (or maybe less than) a few nanometres, which strongly indicates that

the diffusive exchange within the mineral volumes can be ignored, and significant mass transport is confined to fluid-filled channels.

However, whether or not the diffusive flux through these media is more efficient for a given element also depends – for simple mass balance reasons – on their volume fraction and on the relative concentrations of the element (Dohmen and Chakraborty, 2003; Dohmen and Milke, 2010). Even in cases where the lattice diffusion coefficient is small, the leakage flux from the fluid or the grain boundary into the adjacent mineral can be significant. Mass transport along dry grain boundaries is not much more efficient than through the mineral lattices, due to the very small volume fraction of grain boundaries – with the exception of highly incompatible elements (Dohmen and Milke, 2010). The solubility of Mg (and other elements) in the fluid has, therefore, an additional control on its mobility during diffusive mass transfer. We apply a grain boundary diffusion model (Mishin and Herzig, 1995) to estimate whether the leakage flux into the minerals can be ignored. The segregation of elements into the grain boundaries (equivalent to a partition coefficient) is explicitly considered, as an extension of the classification scheme of Harrison (1961). According to this model the bulk diffusivity is dominated by grain-boundary diffusion (Fig. 8 in Dohmen and Milke 2010), if $s \cdot \delta/(2d) \cdot D_{gb}/ D_l >>1$, where s denotes the segregation coefficient, d the grain size, and δ the grain boundary width. Since the mathematics would be equivalent if we replaced the grain boundary diffusion medium by a fluid diffusion medium, we set $D_{gb} = D_{fluid} = 10^{-8} -10^{-9}$ m^2/s for Mg^{2+} (Oelkers and Helgeson, 1988) for a temperature of ~400 °C and a pressure of 0.5 GPa.

The width of the fluid channel (the geometry of the grain boundary triple junction) is on the order of 1 μm, and significantly larger than a grain boundary width,

which is generally estimated to be a few nm. The least-known parameter here is the

fluid-mineral partition coefficient of Mg. Here we use solubilities of Mg reported in

Manning (2004) as proxies – 100 mmol/kg H_2O for zone V and 5 mmol/kg H_2O in

zone I. From the MgO contents and the bulk-rock densities reported in Miller et al.

(2009) we can derive a fluid to bulk-rock partition coefficient for Mg on the order of

10^{-3}. Using this number, we obtain values for $s \cdot \delta/2 \cdot D_{gb}/ D_l$ on the order of 10^{10}

indicating that even on the basis of our poorly constrained parameters we can ignore

the contribution of the lattice diffusion to the bulk flux. We can further conclude that

lattice diffusion would be a very inefficient way for the exchange of the Mg isotopes

between the fluid and chlorite.

The time necessary to form the reaction zone can be calculated from the

integrated flux of MgO required, as is performed in our diffusion model. Since the

fluid network is the dominant diffusion pathway, the integrated flux of MgO, leading

to the formation of the various layers, depends on five factors: the chemical gradient,

the diffusion coefficient and the solubility of Mg in the fluid, the volume fraction or

cross sectional area of the fluid channel, and finally the total time until the system was

frozen. The solubility of Mg depends on many factors such as temperature, pH etc.

and can be in fact very small (e.g., see thermodynamic calculations for a granulite

phase assemblage in Dohmen and Chakraborty 2003). In contrast the diffusion

coefficients of aqueous species in fluids are quite similar and show a very weak

temperature dependence (Oelkers and Helgeson, 1988; Watson and Baxter, 2007).

Consequently, the different relative mobilities and integrated fluxes of the various

oxide components are caused by their different fluid solubilities (Frantz and Mao,

1976; Ketcham and Carlson, 2012). LILE and SiO_2 are therefore the most mobile

components, even if the system is controlled by diffusive flux only and not by

advective flux. The present sequence in the metasomatic reaction zone indicates that Mg was mobile, but Si, Ca, and Na were even more mobile. In contrast, Ti and Al were almost immobile. Hence, we can conclude that Mg was much more soluble than Al or Ti but less soluble than Si, Na, and Ca. This can be demonstrated by a mass balance, based on the assumption that Al_2O_3 is immobile (Miller et al., 2009). The calculation results in a 50% depletion of SiO_2, and an enrichment of 300 to 500% MgO in the chlorite schist, as well as an enrichment of CaO to 140 % in Zone II and 200 % in Zone III. Further, the total mass of elements lost or gained from Zones II, III and IV can be calculated using the rock densities, the thickness of each zone, and the mass loss/gain of each element using the composition of the protolith (Zone I). The results show that a total of 203 kg/m^2 SiO2 was lost from the 40 cm thick blackwall (Zones II-IV), and 125 kg/m^2 MgO was gained (Fig. 11). From the reactions Atg + $2SiO_2$ = Tlc + H_2O and 2Atg = Tlc + 3MgO + $3H_2O$, the release of this amount of SiO_2 and MgO could lead to the formation of a 18–22 cm thick layer of talc each. Thus, in a closed system with no contact-parallel fluid transport, there should be a talc layer ~40 cm thick, rather than the mm-thick layer actually observed. This strongly suggests that Si was leached from the blackwall by advecting fluids, requiring the dissolution of serpentine, by the reaction Atg = 3MgO + $2SiO_2$ + $2H_2O$. To produce 125kg/m^2 MgO, therefore, an ~11cm thick layer of serpentine would require dissolution, providing 37kg/m^2 of H_2O. However, the blackwall gained 46 kg/m^2 of H_2O, meaning that external influx of H_2O is required.

5.5 Constraints for the origin of the δ^{26}Mg anomaly

To explain the observed δ^{26}Mg values, interaction between fluid and minerals in the reaction zone must have been confined to certain zones, with attainment of only local

equilibrium. This strongly points to kinetic controls on fluid-mineral exchange in the reaction zone. Grain-boundary network diffusion would (in contrast to purely advective fluid flux) create an isotopically heterogeneous fluid. This case can be further subdivided into two different situations depending on the mechanism of equilibration: a) Equilibration with the fluid occurs during the reaction by mineral replacement (Putnis, 2009); b) Equilibration with the fluid postdates the formation of the minerals and occurs by diffusion through the mineral volumes. The discussion above on diffusion coefficients for the minerals argues against the latter possibility. However, these two cases would imply different constraints for the amount and local distribution of the fluid as a function of time. In both cases, the δ^{26}Mg profile across the reaction zone would reflect the Mg isotope composition of the fluid (i.e. bulk rock δ^{26}Mg would mirror fluid δ^{26}Mg), given that the major mineral hosts of Mg in the reaction zone do not show Mg isotopic fractionation amongst each other (similar to other studies of the offset between such minerals (Li et al., 2011); Fig. 9). Assuming local isotopic equilibrium between the fluid and the minerals this would imply for case b) that the spatial distribution of δ^{26}Mg in the fluid was identical to that finally obtained across the different zones. Since the low δ^{26}Mg zone is located within the dominant metasomatic zone, it seems more likely that both the formation of the reaction zone and the negative anomaly were created by the same process and at the same time. In this case (case a) only those minerals would be affected that are newly formed by the mineral replacement reaction in the presence of fluid. The isotopic composition of these minerals would result from the mass balance with the fluid as defined by the reaction stoichiometry. For example, considering reaction 3, 1 MgO from diopside is combined with 8 MgO from the fluid to form chlorite. Thus, the Mg isotope composition of the chlorite is dominated by the fluid, which can be supported

by a more detailed mass balance calculation: we assume that the growth of chlorite and omphacite is produced by the uptake of MgO from the fluid at the layer contacts as discussed above. The isotopic composition of the newly formed minerals is then the result of the mass balance between the reaction partners. Assuming a constant and low δ^{26}Mg value for the fluid and a constant but relatively high δ^{26}Mg value of the solid reactants (as given by the garnet-glaucophane schist, ~ -0.2‰) the resulting composition at each point along the profile can be calculated using the amount of MgO to be added from the fluid to reach the measured MgO content (Fig. 5):

$$\delta^{26}Mg^{final} = (MgO^{initial}/MgO^{final})\ \delta^{26}Mg^{solid} + ((MgO^{final} - MgO^{initial})/MgO^{final})\ \delta^{26}Mg^{fluid}$$

This model results in good agreement with the observed δ^{26}Mg profile when we assume $\delta^{26}Mg^{fluid} = -1.2$ ‰ (Fig. 5). In this case, MgO has been transferred from the serpentinite zone through the fluid network into the reaction zone, but the isotopic composition was changed during this transfer, most probably due to diffusive fractionation. The Mg source (the serpentinite) would then be slightly depleted in the light isotopes, which is what we observe, and which also explains samples with high chlorite and high δ^{26}Mg (Fig. 8).

To summarise, we are left with only one possibility as explanation for the Mg isotope anomaly: transfer of isotopically light Mg from the fluid into the minerals during the metasomatic reactions controlled by the diffusive flux of MgO through the fluid network, so that the rate of chlorite formation is directly coupled to the diffusive flux of Mg in the fluid. In this case, diffusive fractionation of the Mg isotopes within the fluid could be the cause of its local isotopically light composition. We have

developed a model to numerically simulate the detailed Mg isotope fractionation in the fluid during the formation of the metasomatic reaction zone.

5.6 Modelling diffusive fractionation of Mg isotopes in a reaction zone

The model. Diffusive fractionation of stable isotopes occurs due to the slightly different diffusion coefficients of the individual isotopes in which light isotopes diffuse faster. A simplified equation to describe the relative diffusivity of two isotopes with masses M_1 and M_2 is given, as follows (Richter et al., 2003; Richter et al., 2008):

$$\frac{D_{M_1}}{D_{M_2}} = \left(\frac{M_2}{M_1}\right)^{\beta} \qquad (7)$$

with β as an empirical coefficient, which depends in principle on the element and the diffusion medium.

The isotopic exchange of the minerals with the fluid occurs effectively during the mineral replacement reactions located at the interfaces of the different zones. We use two infinite plane sheets (finite dimension along the x-axis, infinite along the y- and z-axes) as our system geometry but with one moving boundary to consider the growth of reaction layer IV (Fig. 10). With this simplification we can use a one dimensional diffusion model for symmetry reasons. The position of the interface between the two plane sheets is denoted by $X_{III/IV}$ and is moving due to a net transfer reaction (e.g., Reaction 3) with a velocity $dX_{III/IV}/dt$. The two different sheets represent the reaction zones II + III and IV and we are effectively only modelling the formation of the chlorite zone (Zone IV).

The growth rate of the individual layers and their chemical composition is controlled by the relative fluxes of the chemical components in the system. A relation

between the fluxes and the velocities of the boundaries can be derived from mass balance for each boundary between two adjacent layers and each chemical component. For example, for the boundary between zones III and IV at position $X_{III/IV}$ and MgO we have:

$$J_{MgO}^{III} + C_{MgO}^{III} \cdot \frac{dX_{III/IV}^{III}}{dt} = J_{MgO}^{IV} + C_{MgO}^{IV} \cdot \frac{dX_{III/IV}^{IV}}{dt} \qquad (8)$$

where J_{MgO}^{III}, J_{MgO}^{IV}, C_{MgO}^{III}, and C_{MgO}^{IV} are the flux (units, e.g., mol/cm^2/s) and concentration (units, e.g., mol/cm^3) of MgO in zone III and IV, respectively. A separate velocity of boundary III/IV must be defined for zone III and IV, if the densities of zones III and IV are different from each other. Equation 8 demonstrates the coupling of the element fluxes and the boundary velocities. For the following we assume that the element fluxes are solely diffusion controlled, and as discussed before, are confined to the intergranular fluid. We ignore the volume change induced by the reaction, which would imply a different value for the position of the interface for the two coordinate systems of the plane sheets (Abart et al., 2004) and could also change the porosity and hence influence the net flux through the fluid. With these assumptions, we obtain the following mass balance equation for boundary III/IV from Equation 8:

$$-D_{Mg^{2+}}^{fluid} \cdot \Theta \cdot \frac{\partial C_{Mg^{2+}}^{fluid}}{\partial x}\bigg|_{x=X_{III/IV}^{III}} + D_{Mg^{2+}}^{fluid} \cdot \Theta \cdot \frac{\partial C_{Mg^{2+}}^{fluid}}{\partial x}\bigg|_{x=X_{III/IV}^{IV}} = \left(C_{MgO}^{IV} - C_{MgO}^{III}\right) \cdot \frac{dX_{III/IV}}{dt} \qquad (9)$$

It should be noted that C_{MgO}^{III}, and C_{MgO}^{IV} are bulk concentrations of MgO in Zone III and Zone IV, respectively, right next to the boundary III/IV, whereas the diffusive flux is proportional to the concentration gradient in the fluid weighted by Θ, i.e. the fraction of fluid filled transport channels (e.g., triple junctions) relative to a unit area of the interface. At the boundary of zones III/IV, a discontinuity for the concentration

of MgO is present (see Fig. 5) defining the difference between $C_{\text{MgO}}^{\text{III}}$ and $C_{\text{MgO}}^{\text{IV}}$, which

is here $6.9 \cdot 10^{-3}$ mol/cm^3 (concentrations in units mol/cm^3 where converted from wt%

using molecular weight of MgO and the rock density as given in Miller et al., 2009).

This difference is related to the metasomatic reaction, e.g., as defined in Equation 3. It

can be inferred from Equation 9 that for a certain growth rate this concentration jump

requires a respective diffusive flux across the boundary. If the growth of the layer is

diffusion controlled (by diffusive flux of MgO and other chemical components) the

thickness of layer IV, Δx_{IV}, follows a parabolic law (e.g., Abart et al., 2009): $\Delta_{x\text{IV}2} =$

$k_{\text{IV}}t$, where k_{IV} is a reaction constant and accordingly it follows that $dX_{\text{III/IV}}/dt =$

$1/2k_{\text{IV}}t^{-1/2}$.

The concentration distribution within the fluid is modelled by the continuity

equation for a one-dimensional diffusion problem with a constant diffusion

coefficient, as given by (Crank, 1975):

$$\frac{\partial C(x,t)}{\partial t} = D_{\text{Mg}} \frac{\partial^2 C(x,t)}{\partial x^2} \qquad (10)$$

Equation 10 applies to each isotope (^{24}Mg, ^{25}Mg, and ^{26}Mg) and each plane sheet.

Here we assume thermodynamically ideal behaviour of the Mg species (either the

relevant species in the fluid, e.g. Mg^{2+} (aq.) or MgCl (aq.), etc. or the thermodynamic

component MgO) to relate the chemical potential gradient in a straightforward way to

the concentration gradient. At the outer boundaries of the system we assume a fixed

concentration, which implicitly means that the concentration of Mg and its isotopes is

buffered by a sufficient flux from the right and into the left side of the system

(positive flux from Zone IV and into Zone I). For the boundary at $x = X_{\text{III/IV}}$ one

condition is given by Equation 9 and the second condition follows from the local

equilibrium at the interface, which implies for the fluid the same concentration at both sides next to the boundary:

$$C_{Mg}^{fluid}(X_{III/IV}^{III}) = C_{Mg}^{fluid}(X_{III/IV}^{IV}) \qquad (11)$$

It should be noted here that even though the overall reaction rate is controlled by diffusion through the interconnected fluid network, the isotopic re-equilibration of the solids with the fluid occurs by the localised dissolution/re-precipitation processes at the interfaces of the reaction zones. Once a mineral (e.g., chlorite) is formed by this process, its isotopic composition becomes frozen due to the inefficient solid-state diffusion rates.

Modelling results. The continuity equation 10 with the boundary conditions 9 and 11 was solved numerically for each Mg isotope using the explicit method of finite differences and the front tracking method to account for the moving boundary (see Appendix and Crank, 1975). The set of input parameters are as follows: Θ was estimated to be within 1×10^{-3} and 4×10^{-4}; $\beta = 0.05$ and 0.1; $D_{Mg} = 10^{-8} - 10^{-9}$ m^2/s; the initial concentration distribution (Mg in the serpentinite zone V and in Zone I, see section 5.4); the reaction constant k_{IV}. The diffusion coefficient was estimated from Oelkers and Helgeson (1988) considering T = 430 °C and P = 1.2 GPa as determined by Miller et al. (2009). Because the data in Oelkers and Helgeson (1988) are only for a maximum pressure of 0.5 GPa and due to the effect of the tortuosity, there is at least an order of magnitude uncertainty of D_{Mg}. The rate constant k_{IV} was varied resulting in different values of the total time required to form the approximately 20 cm thick Zone IV. Examples of calculations in this parameter space are illustrated in Fig. 12.

A quasi steady state is reached after time scales of only a few years due to the relatively fast diffusivity in the fluid (Fig. 12). In this steady state a linear concentration gradient for the total Mg in both plane sheets of the model has

developed (e.g., Fig. 12a) and also the profile for $\delta^{26}Mg$ has a stable shape (e.g., Fig. 12b). At the interface between zone III and zone IV a kink appears in the concentration profile as well as in the isotope profile. The difference in the Mg concentration gradient (the slope) between zone III and zone IV is a direct consequence of Equation 9. The concentration gradient in zone IV is larger than in zone III and the difference in the corresponding diffusion fluxes is compensated by the formation of new chlorite and hence growth of zone IV. Because of this mass balance constraint, the difference between these slopes is directly coupled to the chosen growth constant. The faster the growth rate, the higher diffusive flux is needed to form faster chlorite, and hence the difference between the slopes needs to be larger according to Eqn. 9 (Fig. 12a-h). Consequently, a critical growth rate exists where the algorithm becomes unstable simply because the maximum possible difference in the diffusive fluxes between the two zones is defined by the initial concentration difference between zone I and zone V. In this limiting case, the growth of Zone IV is solely controlled by the diffusive flux of MgO and the growth rate, as described here by $dX_{III/IV}/dt$, can be directly derived from Equation 9. Assuming a steady-state flux (linear concentration gradient in each zone for this model geometry) and that the diffusive flux of MgO in Zone III is significantly smaller than in Zone IV, Equation 9 can be integrated to obtain the classical parabolic rate law for diffusion-controlled layer growth:

$$\Delta x^2 = 2 D_{Mg^{2+}}^{fluid} \cdot \Theta \cdot \frac{C_{Mg^{2+}}^{fluid}(X_{IV/V}^{IV}) - C_{Mg^{2+}}^{fluid}(X_{III/IV}^{IV})}{C_{MgO}^{IV} - C_{MgO}^{III}} \cdot t \qquad (12)$$

This relation defines the upper boundary for the growth constant, which is consistent with the mass balance constraint at the interface of zone III/IV given by Equation 9. For the set of input parameters used in Fig. 12 the maximum growth rate is 2.75×10^{-10}

cm^2/s, which is very close to those chosen in panels a and b in Fig. 12. The concentration gradients in zones III and IV become effectively identical, if the growth constant is much smaller, (Fig. 12 c, e, g), which would be equivalent to a situation where the flux of other chemical components control the growth rate of Zone IV. In the extreme case, the diffusive fractionation of the Mg isotopes would be eliminated as illustrated in Fig. 12h.

The most relevant result of this simulation is that the value for δ^{26}Mg is almost constant at the moving boundary (relative to the δ^{26}Mg variations caused by diffusion) for a range of values for the growth constant k_{IV}, where the growth is at least partly controlled by diffusion of Mg. This is expected to be reflected by the isotope composition of Mg that is incorporated into the chlorite formed at the respective position. Therefore, according to this model, the entire chlorite zone would have a δ^{26}Mg composition that changes only subtly with time and profile position. The final isotope profile and the maximum negative δ^{26}Mg anomaly depend not only on the value of β (e.g., compare Fig. 13b with Fig. 12d) but also very strongly on the concentration gradient (e.g., Fig. 13h). To obtain a value of approximately -1.0 for δ^{26}Mg (for β = 0.05), the concentration within the fluid has to change by more than one order of magnitude from the serpentinite zone to the garnet-glaucophane schist. Our estimated values for the Mg concentration covers roughly the range for the solubility reported for Mg (Manning, 2004) – 100 mmol/kg H_2O for Zone V and 5 mmol/kg H_2O in Zone I.

The shape of the profile does not reveal any strong indication for the overall time scale of its formation process due to the steady-state mechanism of growth. However, the thickness of Zone IV, which is, at least partly, controlled by the diffusive flux of MgO to produce diffusive fractionation of the Mg isotopes, does

yield such temporal information. From Equation 12 and our set of input parameters, we can infer that a total time of about 100 kyr is required to form the observed thickness of Zone IV. Uncertainty on this estimate could be up to a factor of 10, given the uncertainties of the input parameters, in particular the Mg concentration in the fluid. It should be noted that without the specific boundary condition given by Eqn. 9, such a large isotopic fractionation would not survive for such a long time, but would be homogenised due to the large diffusion coefficients of Mg in the fluid, as occurs if the growth rate is too small (Fig. 12h). It is the flux from the fluid to the newly formed solids (e.g., chlorite), which act as a significant sink and thereby buffer the isotopic anomaly during layer growth. Note that the duration of reaction zone growth could be constrained much better if the parameter β and the concentration gradient in the fluid would be better constrained. This would require data on solubility and speciation of elements at the relevant pressure and temperature in equilibrium with natural rock compositions.

In any case, in this context ~100 kyr is unlikely to be the time that the two original lithologies (Zones I and V) spent in contact with each other at ~430°C. Instead, it is probably the duration of the presence of grain-boundary fluids in the contact zone. This supports the hypothesis that fluid generation in subduction zones is short lived (John et al., 2012). There certainly was fluid flux parallel to the contact at some stage(s) during formation of the blackwall. This is evident from the bulk loss of SiO_2 and other elements, and from the precipitation of metasomatic tourmaline. Yet, the low viscosity of hydrous fluids at high pressures (Audétat and Keppler, 2004; Hack and Thompson, 2011) suggests that those fluids would flow relatively fast. Hence, if the 100 kyr duration of fluid saturation would have been achieved by constant fluid flux, it would require very large quantities of fluids (on the order of 10^7

cm^3/cm^2. Such large quantities of fast-flowing fluids would also establish a fluid-buffered assemblage and flush out and homogenise any patterns caused by diffusion across the lithological contact. The alternative suggestion is that the reaction zone experienced long periods during which the fluid stagnated (flux of $<10^4$ cm^3/cm^2) and diffusive element transport and reaction zone growth dominated. The hydrous fluid present during these periods does not necessarily need to be of a significant volume. It is only required to wet the grain boundaries and form a network that facilitates diffusion of soluble chemical species.

5.7 Significance of major element diffusion

This study shows unequivocally that Mg is able to diffuse on a dm scale, imparting changes to elemental concentrations and isotope ratios on geologically short timescales. This transport of chemical components is expected to have a limited effect on bulk transfer processes in subduction zones, but diffusion processes arguably have a significant effect on the composition of samples from heterogeneous metamorphic terrains. Thus "snap-shot" sampling of metamorphic zones can yield Mg concentrations and importantly isotope ratios that are unrelated to equilibrium processes, which can therefore lead to a gross misinterpretation of geochemical signals, as has been discussed for Li isotopes (Marschall et al., 2007), and is now shown here to apply to major elements. This also implies that the interpretation of monomineralic zones in general is more complex than previously envisioned (Curtis and Brown, 1969; Koons, 1981), as we show that the approximately constant $\delta^{26}Mg$ in the chlorite zone is due to a layer-by-layer formation of the zone during reaction at the growing zone boundary.

Chlorite schist probably forms in large quantities at the slab-mantle interface and overlying mantle wedge due to the juxtaposition of crustal rocks with hydrated peridotite (Marschall and Schumacher, 2012). Extrapolation from our data suggests that active subduction over ~10^7 years will produce several meters of chlorite schist from boulders of crustal material incorporated into the subduction channel (e.g. subduction over ~65 Myr (Krebs et al., 2008) would completely convert boulders with a radius ≤5.1 m into chlorite schist by diffusion). Higher temperatures will further increase the efficiency of this process. Hence, it is predicted that diffusion, as well as mechanical mixing and deformation, plays a vital role in the homogenisation of the fore-arc mantle wedge in active subduction systems.

Further, diffusion in solids is thought to be sluggish at low temperatures, and therefore not to play a role in rocks on the outcrop scale. However, the presence of fluids and strong chemical gradients enable kinetic fractionation of stable isotopes in whole-rock samples to be very efficient at relatively low temperatures, and to exert an important role in elemental transfer and mineral growth. These data also imply that major elements can diffuse between reservoirs of other high temperature systems, significantly altering their isotope ratios on scales of μm to m. Thus diffusion and kinetic isotope fractionation could occur between mantle xenoliths stored or emplaced in lava (Pogge von Strandmann et al., 2011), between juxtaposed felsic and mafic rocks (Chopra et al., 2012), as well as between rising magma and the mantle wall rock it is interacting with (e.g. formation of dunite channels). Clearly, observing and understanding these processes is of critical importance in the interpretation of stable isotope systems of both major and minor elements in many high temperature magmatic and metamorphic systems.

6.0 Conclusions

This study has analysed Mg isotopes in combination with O isotopes from bulk rocks and mineral separates across a profile spanning the slab-mantle interface from the mélange zone in Syros, Greece. This interface shows a strong MgO concentration gradient, and concomitantly, isotopically very light Mg for a portion of the mélange zone. Mineral separate analyses demonstrate that inter-mineral equilibrium fractionation from a buffered fluid cannot be the cause of the isotopically light Mg isotope ratios. Equally, combined $\delta^{26}Mg$ and $\delta^{18}O$ values demonstrate that the signal cannot stem from equilibration with advective fluid flow.

Kinetic isotope fractionation due to Mg diffusion along the Mg chemical activity gradient is the most likely cause of the observed isotope fractionation. The metamorphic temperatures in the mélange zone were too low (~430°C) for diffusion through the crystal lattices to cause the profile. However, diffusion through an interconnected pore fluid network is conceivably rapid enough. Grain-boundary network diffusion would (in contrast to purely advective fluid flux) create an isotopically heterogeneous fluid that has light isotope ratios at the boundary of the minerals (dominantly chlorite) growing by diffusive supply of Mg. Chlorite growing by this method would gain most of its Mg from the pore fluids, and would be approximately isotopically homogeneous (and isotopically light), because the chlorite only grows at the moving metamorphic boundary. The growth of the chlorite zone is rate-limited by Mg diffusion, suggesting that the interpretation of monomineralic zones in general is exceedingly complex.

This study presents a novel detailed diffusive model of these processes, which can numerically re-create the observed Mg concentrations and isotope ratios. With our input parameters, a total time of ~100 kyr is required to form the isotopic profile and

grow the chlorite zone. Instead of reflecting the time the original lithologies spent in contact at ~430°C, this probably represents the duration of grain-boundary fluid presence, supporting the hypothesis that fluid generation in subduction zones occurs in relatively short-lived pulses compared to the time scales of subduction and exhumation.

Hence the data and model show that Mg is able to diffuse on a metre scale, and that chlorite schists in subduction zones are likely to form by this process. Boulders of crustal material of over 10 m in diameter could be converted to chlorite within ~65 Myr by diffusion, providing another mechanism in addition to mechanical and advective mixing by which the fore-arc mantle wedge can homogenise. In addition, the data suggest that "snap-shot" sampling of metamorphic zones (or indeed erupted mantle xenoliths) will not yield equilibrium Mg concentrations or isotope ratios, potentially leading to misinterpretation of these rocks.

Abart, R., Kunze, K., Milke, R., Sperb, R., and Heinrich, W., 2004, Silicon and oxygen self diffusion in enstatite polycrystals: the Milke et al. (2001) rim growth experiments revisited: Contributions to Mineralogy and Petrology, v. 147, no. 6, p. 633-646.

Abart, R., Petrishcheva, E., Fischer, F. D., and Svoboda, J., 2009, Thermodynamic model for diffusion controlled reaction rim growth in a binary system: application to the forsterite-enstatite-quartz system: American Journal of Science, v. 309, no. 2, p. 114-131.

Ashworth, J. R., and Birdi, J. J., 1990, Diffusion modeling of coronas around olivine in an open system: Geochimica Et Cosmochimica Acta, v. 54, no. 9, p. 2389-2401.

Audétat, A., and Keppler, H., 2004, Viscosity of fluids in subduction zones: Science, v. 202, p. 513–516.

Bach, W., Jons, N., and Klein, F., 2013, Metasomatism within the oceanic crust, *in* Harlov, D. E., and Austrheim, H., eds., Metasomatism and the Chemical Transformation of Rock, p. 253–288.

Bebout, G. E., 2012, Metasomatism in subduction zones of subducted oceanic slabs, mantle wedges, and the slab-mantle interface, *in* Harlow, D. E., and Austrheim, H., eds., Metasomatism and the Chemical Transformation of Rock, Springer, p. 289-350.

Bourdon, B., Tipper, E. T., Fitoussi, C., and Stracke, A., 2010, Chondritic Mg isotope composition of the Earth: Geochimica Et Cosmochimica Acta, v. 74, p. 5069-5083.

Breeding, C. M., Ague, J. J., and Bröcker, M., 2004, Fluid–metasedimentary rock interactions in subduction-zone melange: Implications for the chemical composition of arc magmas: Geology, v. 32, no. 12, p. 1041-1044.

Brocker, M., and Enders, M., 2001, Unusual bulk-rock compositions in eclogite-facies rocks from Syros and Tinos (Cyclades, Greece): implications for U-Pb zircon geochronology: Chemical Geology, v. 175, no. 3-4, p. 581-603.

Carmody, L., Barry, P. H., Shervais, J. W., Kluesner, J. W., and Taylor, L. A., 2013, Oxygen isotopes in subducted oceanic crust: A new perspective from Siberian diamondiferous eclogites: Geochemistry Geophysics Geosystems, v. in press.

Chakraborty, S., 1997, Rates and mechanisms of Fe-Mg interdiffusion in olivine at 980 degrees-1300 degrees C: Journal of Geophysical Research-Solid Earth, v. 102, no. B6, p. 12317-12331.

Cherniak, D. J., 1996, Strontium diffusion in sanidine and albite, and general comments on strontium diffusion in alkali feldspars: Geochimica Et Cosmochimica Acta, v. 60, no. 24, p. 5037-5043.

Chopra, R., Richter, F. M., Watson, E. B., and Scullard, C. R., 2012, Magnesium Isotope Fractionation By Chemical Diffusion In Natural Settings And In Laboratory Analogues: Geochimica Et Cosmochimica Acta, v. 88, p. 1-18.

Connolly, J. A. D., 2005, Computation of phase equilibria by linear programming: A tool for geodynamic modeling and its application to subduction zone decarbonation: Earth and Planetary Science Letters, v. 236, p. 524–541.

-, 2009, The geodynamic equation of state: what and how. : Geochemistry, Geophysics, Geosystems, v. 10:Q10014.

Crank, J., 1975, The Mathematics of Diffusion, Oxford University Press.

Curtis, C. D., and Brown, P. E., 1969, Metasomatic development of zoned ultabasic bodies in Unst, Shetland: Contributions to Mineralogy and Petrology, v. 24, no. 4, p. 275-&.

Dauphas, N., Teng, F. Z., and Arndt, N. T., 2010, Magnesium and iron isotopes in 2.7 Ga Alexo komatiites: Mantle signatures, no evidence for Soret diffusion, and identification of diffusive transport in zoned olivine: Geochimica Et Cosmochimica Acta, v. 74, p. 3274-3291.

Desmons, J., and O'Neil, R., 1978, Oxygen and Hydrogen Isotope Compositions of Eclogites and Associated Rocks from the Eastern Sesia Zones (Western Alps, Italy): Contributions to Mineralogy and Petrology, v. 67, p. 79–85.

Dohmen, R., and Chakraborty, S., 2003, Mechanism and kinetics of element and isotopic exchange mediated by a fluid phase: American Mineralogist, v. 88, no. 8-9, p. 1251-1270.

Dohmen, R., and Milke, R., 2010, Diffusion in Polycrystalline Materials Grain Boundaries, Mathematical Models, and Experimental Data, *in* Zhang, Y. X., and Cherniak, D. J., eds., Diffusion in Minerals and Melts, Volume 72, p. 921-970.

Dürr, S., Altherr, R., Keller, J., Okrusch, M., and Seidel, E., 1978, The median Aegean crystalline belt: stratigraphy, structure, metamorphism, magmatism, *in* Closs, H., Roeder, D. H., and Schmidt, K., eds., Also, Apennines, Hellenides, Volume 38.

Eiler, J. M., Valley, J. W., and Stolper, E. M., 1996, Oxygen isotope ratios in olivine from the Hawaii Scientific Drilling Project: Journal of Geophysical Research (B), v. 101, p. 11807–11813.

Elliott, T., Jeffcoate, A., and Bouman, C., 2004, The terrestrial Li isotope cycle: light-weight constraints on mantle convection: Earth and Planetary Science Letters, v. 220, no. 3-4, p. 231-245.

Fisher, G. W., 1973, Nonequilibrium thermodynamics as a model for diffusion-contolled metamorphic processes: American Journal of Science, v. 273, no. 10, p. 897-924.

Frantz, J. D., and Mao, H. K., 1976, BIMETASOMATISM RESULTING FROM INTERGRANULAR DIFFUSION .1. THEORETICAL-MODEL FOR MONOMINERALIC REACTION ZONE SEQUENCES: American Journal of Science, v. 276, no. 7, p. 817-840.

Fukuyama, M., Nishiyama, T., Urata, K., and Mori, Y., 2006, Steady-diffusion modelling of a reaction zone between a metamorphosed basic dyke and a marble from Hirao-dai, Fukuoka, Japan: Journal of Metamorphic Geology, v. 24, no. 2, p. 153-168.

Gallagher, K., and Elliott, T., 2009, Fractionation of lithium isotopes in magmatic systems as a natural consequence of cooling Earth and Planetary Science Letters, v. 278, p. 286-296.

Galy, A., Yoffe, O., Janney, P. E., Williams, R. W., Cloquet, C., Alard, O., Halicz, L., Wadhwa, M., Hutcheon, I. D., Ramon, E., and Carignan, J., 2003, Magnesium isotope heterogeneity of the isotopic standard SRM980 and new reference materials for magnesium-isotope-ratio measurements: Journal of Analytical Atomic Spectrometry, v. 18, no. 11, p. 1352-1356.

Gardes, E., and Heinrich, W., 2011, Growth of multilayered polycrystalline reaction rims in the MgO-SiO2 system, part II: modelling: Contributions to Mineralogy and Petrology, v. 162, no. 1, p. 37-49.

Gardes, E., Wunder, B., Wirth, R., and Heinrich, W., 2011, Growth of multilayered polycrystalline reaction rims in the MgO-SiO2 system, part I: experiments: Contributions to Mineralogy and Petrology, v. 161, no. 1, p. 1-12.

Hack, A. C., and Thompson, A. B., 2011, Density and viscosity of hydrous magmas and related fluids and their role in subduction zone processes: Journal of Petrology, v. 52, p. 1333–1362.

Handler, M. R., Baker, J. A., Schiller, M., Bennett, V. C., and Yaxley, G. M., 2009, Magnesium stable isotope composition of Earth's upper mantle: Earth and Planetary Science Letters, v. 282, p. 306-313.

Harrison, L. G., 1961, Influence of Dislocations on Diffusion Kinetics in Solids with Particular Reference to Alkali Halides: Transactions of the Faraday Society, v. 57, no. 8, p. 1191-&.

Hecht, J., 1984, Geological map of Greece 1:50,000, Syros Island: Institute of Geology and Mineral Exploration, Athens.

Jeffcoate, A. B., Elliott, T., Kasemann, S. A., Ionov, D., Cooper, K., and Brooker, R., 2007, Li isotope fractionation in peridotites and mafic melts: Geochimica Et Cosmochimica Acta, v. 71, no. 1, p. 202-218.

Joesten, R., 1977, Evolution of mineral assemblage zoning in diffusion metasomatism: Geochimica Et Cosmochimica Acta, v. 41, no. 5, p. 649-670.

John, T., Gussone, N., Podladchikov, Y. Y., Bebout, G. E., Dohmen, R., Halama, R., Klemd, R., Magna, T., and Seitz, H. M., 2012, Volcanic arcs fed by rapid pulsed fluid flow through subducting slabs: Nature Geoscience, v. 5, no. 7, p. 489-492.

Keiter, M., Ballhaus, C., and Tomaschek, F., 2011, A new geological map of the Island of Syros (Aegean Sea, Greece): implications for lithostratigraphy and structural history of the Cycladic Blueschist Unit: Geological Society of America Special Paper, v. 481, p. 43pp.

Keiter, M., Piepjohn, K., Ballhaus, C., Lagos, M., and Bode, M., 2004, Structural development of high-pressure metamorphic rocks on Syros island (Cyclades, Greece): Journal of Structural Geology, v. 26, no. 8, p. 1433-1445.

Ketcham, R. A., and Carlson, W. D., 2012, Numerical simulation of diffusion-controlled nucleation and growth of porphyroblasts: Journal of Metamorphic Geology, v. 30, no. 5, p. 489-512.

Koons, P. O., 1981, A study of natural and experimental metasomatic assemblages in an ultramafic-quartzofeldspathic metasomatic system from the Haast Schist, South Island, New-Zealand: Contributions to Mineralogy and Petrology, v. 78, no. 2, p. 189-195.

Krebs, M., Maresch, W. V., Schertl, H.-P., Münker, C., Baumann, A., Draper, G., Idleman, B., and Trapp, E., 2008, The dynamics of intra-oceanic subduction zones: A direct comparison between fossil petrological evidence (Rio San Juan Complex, Dominican Republic) and numerical simulation: Lithos, v. 103, p. 106-137.

Li, W. Y., Teng, F. Z., Xiao, Y., and Huang, J., 2011, High-temperature inter-mineral magnesium isotope fractionation in eclogite from the Dabie orogen, China: Earth and Planetary Science Letters, v. 304, p. 224-230.

Manning, C. E., 2004, The chemistry of subduction-zone fluids: Earth and Planetary Science Letters, v. 223, p. 1–16.

Marschall, H. R., Ludwig, T., Altherr, R., Kalt, A., and Tonarini, S., 2006, Syros metasomatic tourmaline: Evidence for very high-delta B-11 fluids in subduction zones: Journal of Petrology, v. 47, no. 10, p. 1915-1942.

Marschall, H. R., Pogge von Strandmann, P. A. E., Seitz, H. M., Elliott, T., and Niu, Y. L., 2007, The lithium isotopic composition of orogenic eclogites and deep subducted slabs: Earth and Planetary Science Letters, v. 262, p. 563-580.

Marschall, H. R., and Schumacher, J. C., 2012, Arc magmas sourced from melange diapirs in subduction zones: Nature Geoscience, v. 5, no. 12, p. 862-867.

Miller, D. P., Marschall, H. R., and Schumacher, J. C., 2009, Metasomatic formation and petrology of blueschist-facies hybrid rocks from Syros (Greece): Implications for reactions at the slab-mantle interface: Lithos, v. 107, no. 1-2, p. 53-67.

Mishin, Y., and Herzig, C., 1995, Diffusion in fine-grained materials: Theoretical aspects and experimental possibilities: Nanostructured Materials, v. 6, no. 5-8, p. 859-862.

Oelkers, E. H., and Helgeson, H. C., 1988, Calculation of the thermodynamic and transport properties of aqueous species at high pressures and temperatures: Aqueous tracer diffusion coefficients of ions to 1000°C and 5 kb: Geochimica Et Cosmochimica Acta, v. 52, p. 63-85.

Okrusch, M., and Brocker, M., 1990, ECLOGITES ASSOCIATED WITH HIGH-GRADE BLUESCHISTS IN THE CYCLADES ARCHIPELAGO, GREECE - A REVIEW: European Journal of Mineralogy, v. 2, no. 4, p. 451-478.

Penniston-Dorland, S. C., Bebout, G. E., Pogge von Strandmann, P. A. E., Elliott, T., and Sorensen, S. S., 2012, Lithium and its isotopes as tracers of subduction zone fluids and metasomatic processes: Evidence from the Catalina Schist, California, USA: Geochimica Et Cosmochimica Acta, v. 77, p. 530-545.

Penniston-Dorland, S. C., Sorensen, S. S., Ash, R. D., and Khadke, S. V., 2010, Lithium isotopes as a tracer of fluids in a subduction zone melange: Franciscan Complex, CA: Earth and Planetary Science Letters, v. 292, no. 1-2, p. 181-190.

Pogge von Strandmann, P. A. E., Elliott, T., Marschall, H. R., Coath, C., Lai, Y. J., Jeffcoate, A. B., and Ionov, D. A., 2011, Variations of Li and Mg isotope ratios in bulk chondrites and mantle xenoliths: Geochimica Et Cosmochimica Acta, v. 75, p. 5247-5268.

Pogge von Strandmann, P. A. E., Opfergelt, S., Lai, Y. J., Sigfusson, B., Gislason, S. R., and Burton, K. W., 2012, Lithium, magnesium and silicon isotope behaviour accompanying weathering in a basaltic soil and pore water profile in Iceland: Earth and Planetary Science Letters, v. 339–340, p. 11–23.

Putnis, A., 2009, Mineral replacement reactions, *in* Oelkers, E. H., and Schott, J., eds., Thermodynamics and kinetics of water-rock interaction, Volume Reviews in Mineralogy and Geochemistry, Mineralogical Society of America, p. 87–124.

Richter, F. M., Davis, A. M., DePaolo, D. J., and Watson, E. B., 2003, Isotope fractionation by chemical diffusion between molten basalt and rhyolite: Geochimica Et Cosmochimica Acta, v. 67, no. 20, p. 3905-3923.

Richter, F. M., Watson, E. B., Mendybaev, R. A., Teng, F. Z., and Janney, P. E., 2008, Magnesium isotope fractionation in silicate melts by chemical and thermal diffusion: Geochimica Et Cosmochimica Acta, v. 72, no. 1, p. 206-220.

Ridley, J., 1984, EVIDENCE OF A TEMPERATURE-DEPENDENT BLUESCHIST TO ECLOGITE TRANSFORMATION IN HIGH-PRESSURE METAMORPHISM OF METABASIC ROCKS: Journal of Petrology, v. 25, no. 4, p. 852-870.

Rosenbaum, G., Avigad, D., and Sanchez-Gomez, M., 2002, Coaxial flattening at deep levels of orogenic belts: evidence from blueschists and eclogites on Syros and Sifnos (Cyclades, Greece): Journal of Structural Geology, v. 24, no. 9, p. 1451-1462.

Rudnick, R. L., and Ionov, D. A., 2007, Lithium elemental and isotopic disequilibrium in minerals from peridotite xenoliths from far-east Russia: Product of recent melt/fluid–rock reaction: Earth and Planetary Science Letters, v. 256, p. 278-293.

Sanford, R. F., 1982, Growth of Ultramafic Reaction Zones in Greenschist to Amphibolite Facies Metamorphism: American Journal of Science, v. 282, p. 543-616.

Seck, H. A., Kotz, J., Okrusch, M., Seidel, E., and Stosch, H. G., 1996, Geochemistry of a meta-ophiolite suite: An association of metagabbros, eclogites and glaucophanites on the island of Syros, Greece: European Journal of Mineralogy, v. 8, no. 3, p. 607-623.

Sorensen, S. S., and Barton, M. D., 1987, Metasomatism and partial melting in a subduction complex: Catalina Schist, southern California: Geology, v. 15, p. 115-118.

Teng, F. Z., Dauphas, N., Helz, R. T., Gao, S., and Huang, S. C., 2011, Diffusion-driven magnesium and iron isotope fractionation in Hawaiian olivine: Earth and Planetary Science Letters, v. 308, no. 3-4, p. 317-324.

Teng, F. Z., Li, W. Y., Ke, S., Marty, B., Dauphas, N., Huang, S., Wu, F.-Y., and Pourmand, A., 2010, Magnesium isotopic composition of the Earth and chondrites: Geochimica Et Cosmochimica Acta, v. 74, p. 4150-4166.

Teng, F. Z., McDonough, W. F., Rudnick, R. L., and Walker, R. J., 2006, Diffusion-driven extreme lithium isotopic fractionation in country rocks of the Tin Mountain pegmatite: Earth and Planetary Science Letters, v. 243, p. 701-710.

Tipper, E. T., Galy, A., and Bickle, M. J., 2006, Riverine evidence for a fractionated reservoir of Ca and Mg on the continents: Implications for the oceanic Ca cycle: Earth and Planetary Science Letters, v. 247, no. 3-4, p. 267-279.

Trotet, F., Vidal, O., and Jolivet, L., 2001, Exhumation of Syros and Sifnos metamorphic rocks (Cyclades, Greece). New constraints on the P-T paths: European Journal of Mineralogy, v. 13, no. 5, p. 901-920.

Vogel, D. E., and Garlick, G. D., 1970, Oxygen-Isotope Ratios in Metamorphic Eclogites: Contributions to Mineralogy and Petrology, v. 28, p. 183–191.

Wang, Z., Bucholz, C., Shimizu, N., and Eiler, J., 2011, Oxygen isotope constraints on the origin of high-Cr garnets from kimberlites: Earth and Planetary Science Letters, v. 312, p. 337–347.

Watson, E. B., 1991, Diffusion in fluid-bearing and slightly-melted rocks: experimental and numerical approaches illustrated by iron transport in dunite: Contributions to Mineralogy and Petrology, v. 107, p. 417-434.

Watson, E. B., and Baxter, E. F., 2007, Diffusion in solid-Earth systems: Earth and Planetary Science Letters, v. 253, p. 307-327.

Zhang, X. Y., Ganguly, J., and Ito, M., 2010, Ca-Mg diffusion in diopside: tracer and chemical inter-diffusion coefficients: Contributions to Mineralogy and Petrology, v. 159, no. 2, p. 175-186.

Zheng, Y. F., 1991, Calculation of oxygen isotope fractionation in metal-oxides: Geochimica Et Cosmochimica Acta, v. 55, no. 8, p. 2299-2307.

-, 1993a, Calculation of oxygen isotope fractionation in anhydrous silicate minerals: Geochimica Et Cosmochimica Acta, v. 57, no. 5, p. 1079-1091.

-, 1993b, Calculation of oxygen-isotope fractionation in anhydrous silicate minerals: Geochimica Et Cosmochimica Acta, v. 57, no. 13, p. 3199-3199.

-, 1996, Oxygen isotope fractionations involving apatites: Application to paleotemperature determination: Chemical Geology, v. 127, no. 1-3, p. 177-187.

Figure captions

Figure 1. Simplified geological map of the northern part of Syros (Keiter et al., 2011). The locality investigated and sampled in this study is located at the western side of northern Syros in the bay of Lia. The schematic sketch depicts the field relations at Lia beach (Syros, Greece) showing the contact between the meta-volcaniclastic schist, the reaction zone and the serpentinite. No single continuous section through the netire contact zone was available, but the three sections (PS I, PS II, PS III) show significant overlap as judged from their field relations and their mineral composition. Together, they cover the full section from the garnet-phengite-epidote-glaucophane schist into the serpentinite. Samples SY551 and SY552 were taken from the interior of the serpentinite body at distances of 5 and 10m, respectively.

Figure 2. An approximately 0.5 km x 4 km large mélange zone is exposed in this part of Syros that comprises serpentinites, metabasic rock and a variety of reaction-zone products, such as tremolite-talc-chlorite-actinolite-rich schists. The field photographs are of the contact between serpentinite and glaucophane schist from Lia beach on Syros. (a) The contact zone between the large serpentinite body (pale green) and the overlying glaucophane schist (dark) is well exposed along the northern end of Lia beach. The dashed white line indicates the initial contact. The reaction zone located above the initial contact is approximately 1 m wide. (b) Close-up on the contact between serpentinite and glaucophane schist with glaucophane and omphacite-bearing zones II and III of the reaction zone protruding as a prominent layer due to their higher resistance to erosion. (c) Sample section PS I representing mostly Zone III and Zone IV rocks. Samples were taken with a rock cutter, which

produced the visible slit (d) Transition from serpentinite at the bottom to chlorite schist (Zone IV) to omphacite-chlorite rock (Zone III) and glaucophane-epidote-chlorite rock (Zone II). Note hammer for scale. (e) Sample section PS III with unaltered garnet-glaucophane schist at the bottom and the transition into the reaction zone. This sample section was also taken using the rock cutter. (f) Sample section PS II showing the transition from serpentinite into Zone IV chlorite schist. Sections PS I and PS II are in direct contact to each other, as indicated in (c) and (f).

Figure 3. Modal composition of samples investigated in this study. Sample IDs and petrographic zones are given. Mineral proportions are given in % by mass, as calculated from mineral and whole rock chemistry and estimated from thin sections. Modified from Miller et al. (2009). Mineral abbreviations following Whitney and Evans (2010) are: Ab = albite, Atg = antigorite, Chl = chlorite, Ep = epidote, Gln = glaucophane, Grt = garnet, Ilm = ilmenite, Omp = omphacite, Opq = opaque phases, Ph = phengite, Rt = rutile, Tlc = talc,Ttn = titanite (= sphene),Tur = tourmaline.

Figure 4. Sequence of photomicrographs depicting the textural and mineralogical changes throughout the reaction zone. All images are oriented with their long axis parallel to the serpentinite-schist contact (E-W), and they are all displayed at the same scale, representing 11.2×8.3mm. Note 2000μm scale bar in all images. (a) Sample A7.1 (Zone I; −0.693m; section PSIII) consisting of glaucophane (Gln; blue, prismatic), phengite (Ph; colorless), epidote (Ep; anhedral beige aggregates with high refractive index), ilmenite (Ilm; opaque), rutile (Rt; small, dark) and garnet (Grt; large, sand-colored, subhedral grains with fractures). Incipient chlorite (Chl; green) formation is evident at the margin and in cracks of the garnet

blasts. (b) Sample A6.1 (Zone I; −0.447m; section PSIII) dominated by Gln and Ep, while chloritization of Grt is more progressed than in A7.1. Ph and Chl are restricted to pseudomorphs after Grt. c) Sample A5.1 (Zone I; −0.420 m; section PSIII) dominated by Gln and Ep, with Grt partially replaced by Chl and Ph. Note the euhedral Gln intergrown with Chl and Ph in the haloes around Grt. Chl also appears in the Ep-Gln matrix. (d) Sample A4.1 (Zone II; −0.366m; section PSIII) dominated by Gln and Ep, with Grt entirely replaced by Chl and Ph. Rt partially replaced by titanite (Ttn). (e) Sample A2.1 (Zone III; −0.285m; section PSIII) dominated by Ep, Chl and omphacite (Omp; short prismatic, pale green, high refractive index) and minor albite (Ab, colorless). Gln is mostly restricted to pseudomorphs after Grt. (f) Sample 10.1 (Zone III; −0.266m; section PSI) dominated by Omp, Ep, Chl, Ab and Ttn. Grt pseudomorphs, Ph and Gln are absent. The texture is isotropic. (g) Sample A2.0 (Zone III; −0.258m; section PSIII) dominated by Chl, Ep, Omp, Ttn and minor Ab. Gln is restricted to some pseudomorphs after Grt. (h) Sample A1.2 (Zone III to IV; −0.234m; section PSIII) shows the transition from Zone III and Zone IV. The upper part of the image (facing sample A2.0 in the profile) shows Ep with Ttn and Chl, while the lower part (facing sample A1.1 in the profile) consists of Chl and Ttn with minor Ab and apatite (Ap; colorless). (i) Sample A1.1 (Zone IV; −0.204m; section PSIII) consists of Chl, Ttn, Rt and Ap. (k) Sample 12.0 (Zone IV; −0.199m; section PSII) consists of Chl, Ttn, Rt and Ap. (l) Sample 13.2 (Zone IV; −0.074 m; section PSII) consists of Chl, Rt and Ap. This sample shows a reduced grain size and stronger foliation compared to 12.0. (m) Sample 13.4 (Zone IV; −0.037m; section PSII) consists of Chl, an opaque phase (Ilm?), Rt and Ap. (n) Sample 14.0 (Zone IV; −0.010m; section PSII) consists of Chl and an opaque phase (Ilm?). Note the decrease in color intensity of the Chl from 12.0 to 14.0 due to an increase Mg/Fe ratio towards

the serpentinite. (o) Sample 15.1 (Zone V; +0.017m; section PSII) consists of antigorite serpentine (Atg), talc (Tlc), Chl and opaque phases (magnetite, chromite?). (p) Sample 15.2 (Zone V; +0.044m; section PSII) consists of Atg, Tlc, Mag and chromite. A Atg-Mag mesh texture is visible in the central and lower left parts of the image, which is typical of undeformed, serpentinized peridotite. (q) Sample 16.0 (Zone V; +0.071m; section PSII) consists of Atg and an opaque phase (magnetite?).

Figure 5. Profile across reaction zone for MgO and δ^{26}Mg. Mass balance δ^{26}Mg was calculated using constant silicate and fluid δ^{26}Mg, and varying the silicate MgO (see text for details). Zone divisions and mineralogy are from Miller et al., 2009, and are described in the text.

Figure 6. O isotopic composition of whole-rock samples through the reaction zone (green) and calculated hydrous fluid in equilibrium with measured whole-rock values (red). Mg isotope profile (blue) displayed for comparison. The green and blue horizontal bars depict the initial compositions of the rocks prior to the formation of the reaction zone.

Figure 7. Whole-rock O vs. Mg isotopic compositions of samples of the different petrographic zones connected by the black line in order of their appearance along the profile. Unaltered serpentinites of Zone V and glaucophane schist of Zone I have very similar δ^{18}O and δ^{26}Mg values, and no correlation exists between O and Mg isotopes throughout the profile.

Figure 8. a) Correlation of bulk silicate δ^{26}Mg with fraction of chlorite in the

rock, and b) correlation of chlorite with MgO. Deviations from linear trends of % chlorite with δ^{26}Mg and MgO suggest that diffusion is operating (see text for details).

Figure 9. Mg isotopic compositions of different mineral separates are similar, and hence rule out equilibrium fractionation of an isotopically light chlorite from a buffered fluid composition as a cause of light whole-rock Mg isotope ratios.

Figure 10. a) Cartoon of the present metamorphic zones; b) Mg concentrations and mineral assemblages at t=0; c) Mg concentrations and mineral assemblages as diffusion progresses; d) Plot of chemical potential (μ) of MgO, Al_2O_3 and SiO_2 for compositions along the measured profile.

Figure 11. Mass balance plot showing the relative influence of variation of whole-rock MgO, SiO_2 and CaO abundances in the reaction zone normalised to the Al_2O_3 abundance of the protolith as represented by sample PSIII-A7 (-69.3 cm). Silica and lime are significantly depleted in Zone IV relative to alumina, whereas magnesia shows a steady increase throughout Zones III and IV. Note different scales for MgO (right axis) and SiO_2 and CaO (left axis). The element abundances in the serpentinite (Zone V) are given relative to their average abundances in the samples at 5 m and 10 m distance from the contact, but not normalised to their Al_2O_3 content due to the low Al content of serpentinite. The arrows on top depict bulk removal of silica from the profile with an increasing amount from Zone II to III to IV. The numerical values are given in kg per square meter of reaction zone cross section. CaO and MgO show a dominant flux across the reaction zone and values are given for the mass transfer at the boundaries between adjacent zones.

Figure 12. Modelled diffusion profiles of Mg (a, c, e, and g) and δ^{26}Mg (b, d, f, h) in the fluid across the melange zone and their evolution with time. For simplification only one moving boundary was introduced, the interface between Zone III and IV, which position can be recognized here by the kink in the concentration and isotope profiles (indicated by an arrow in a and b). The Mg and δ^{26}Mg concentration profile shows a quasi-steady state shape with a linear concentration gradient within the two different diffusion media and a roughly constant concentration at the interface. The four sets of figures for Mg and δ^{26}Mg illustrate the effect of variable growth rates (as defined by the growth constant k_{IV}) for otherwise constant input parameters as displayed in an onset of Fig. 12a. With decreasing growth constant (and correspondingly longer time scales of evolution) the kink at the interface for Mg becomes less pronounced and the isotope anomaly becomes smaller. The model results in panel c and d are for a case where we obtain roughly constant values of around -1.3‰ for δ^{26}Mg at the interface between zone III and IV.

Figure 13. Same type of diagrams as shown in Fig. 12 illustrating the effects of other input parameters than k_{IV} on the magnitude of the isotope anomaly observed. In panel a and b a larger β was chosen compared to panel c and d in Fig. 12 producing a larger isotope anomaly by roughly a factor of 2. In panel c and d D_{Mg} is one order of magnitude faster compared to the other cases illustrated, reducing basically the time scale by a factor of 10 (compare with panel c and d in Fig. 12). In panel e and f the porosity was reduced, which correspondingly increases the time scale to obtain he same rim width (compare with Eqn. 12) and the same magnitude for the isotope anomaly. In panel g and h the concentration gradient was reduced (solubility of Mg in

the serpentinite zone), which also increases the time scale to obtain the same rim width and isotope anomaly.

Zone	Zone I (Gln+Ep+Grt+Phe)	Zone II (Gln+Ep+Chl)		Zone III (Omp-Ep-Chl)			Zone IV (chlorite schist)						Zone V (serpentinite)			
Sample	PSIII A7	PSIII A4.2	PSIII A2.2	PSIII A2.1	PSI 10.1	PSIII A2.0	PSIII A1.1	PSI 11.2	PSII 12.0	PSII 13.2	PSII 13.4	PSII 14.0	PSII 15.2	PSII 16.0	SY551	SY552
Modes																
Gln	64	51	45	5		1										
Ep	20	30	25	45	28	32	1	5.5								
Phe	10.8	0.2														
Chl	2	10	8	22	24	45	95	87	97	98	97	97.5	0	0	0	0
Grt	1															
Rt	1.27	0.5					0.81	0.8	1.77	1.5	0.1	0.1				
Ttn		2.19	3.07	2.6	3.35	3.25	2.5	3.2	0.21							
Opq	1	4						4			2.29	1.97	5	3	3	4
Ap	0.37	0.26	0.21	0.13	0.08	0.08	0.095	0.07	0.5	0.28	0.3	0.03	0.01	0.02	0.02	0.02
Tur		1	8													
Ab			3	10	15											
Cpx			8	15	30	18										
Atg													90	97	97	96
Tlc													5			
Other									Mnz							
Total	100.44	99.15	100.28	99.73	100.43	99.33	99.41	100.57	99.48	99.78	99.69	99.60	100.01	100.02	100.02	100.02

Table 1. Modal abundances (by mass) of samples investigated in this study. Mineral proportions are given in % by mass, as calculated from mineral and whole-rock chemistry and estimated from thin sections. Modified from Miller et al. (2009). See Fig. 2 for mineral abbreviations.

Zone	Zone I (Gln+Ep+Grt+Phe)	Zone II (Gln+Ep+Chl)		Zone III (Omp Ep Chl)			Zone IV (chlorite schist)						Zone V (serpentinite)			
Sample	PSIII A7	PSIII A4.2	PSIII A2.2	PSIII A2.1	PSI 10.1	PSIII A2.0	PSIII A1.1	PSI 11.2	PSIII 12.0	PSIII 13.2	PSIII 13.4	PSIII 14.0	PSIII 15.2	PSIII 16.0	SY551	SY552
Distance (m)	-0.695	-0.393	-0.312	-0.285	-0.266	-0.258	-0.204	-0.200	-0.199	-0.074	-0.047	-0.010	0.044	0.071	5.000	10.000
Miller et al., 2009 (m)	0.027	0.327	0.408	0.435	1.299	0.462	0.516	1.365	1.380	1.505	1.542	1.569	1.623	1.650	5.000	10.000
SiO2	50.17	46.03	48.00	43.06	46.49	38.54	27.80	27.17	28.14	30.09	31.01	31.38	40.23	40.38	40.94	40.58
TiO2	1.29	1.39	1.30	1.04	1.34	1.30	1.81	2.08	1.84	1.50	1.25	1.08	0.02	0.06	0.07	0.03
Al2O3	14.87	14.70	14.07	15.02	14.12	16.19	18.29	18.35	18.42	17.84	15.12	14.30	1.39	2.15	2.71	2.87
Fe2O3	11.88	13.59	12.95	13.21	8.66	14.41	16.80	17.40	11.64	9.59	8.47	8.26	10.31	7.62	7.96	8.33
MnO	0.17	0.15	0.15	0.17	0.15	0.18	0.21	0.21	0.14	0.10	0.07	0.06	0.13	0.09	0.10	0.09
MgO	6.95	7.47	7.51	7.75	10.01	10.71	21.86	20.94	26.76	30.29	31.35	32.80	34.54	34.95	34.71	34.63
CaO	5.80	8.15	8.01	12.17	10.80	10.52	1.39	2.19	0.34	0.17	0.18	0.04	0.04	0.05	0.04	0.04
Na2O	4.65	3.91	4.42	3.70	4.79	2.36	0.06	0.00	0.05	0.00	0.04	0.00	0.01	0.00	0.01	0.00
K2O	1.11	0.04	0.03	0.02	0.05	0.01	0.00	0.00	0.00	0.01	0.01	0.01	0.01	0.01	0.01	0.01
P2O5	0.15	0.11	0.09	0.05	0.05	0.05	0.04	0.05	0.26	0.12	0.13	0.01	0.01	0.01	0.01	0.01
Cr2O3	0.00	0.00	0.01	0.01	0.03	0.01	0.02	0.01	0.04	0.04	0.03	0.03	0.67	0.38	0.36	0.40
NiO	0.00	0.00	0.00	0.00	0.01	0.01	0.01	0.00	0.02	0.02	0.02	0.07	0.31	0.26	0.31	0.33
LOI	2.05	2.72	2.29	3.21	2.79	4.95	10.19	11.61	11.18	9.68	11.90	11.93	11.27	11.80	11.36	11.29
Total	99.05	98.26	98.80	99.41	99.26	99.23	98.48	99.59	98.82	99.95	99.57	99.97	98.94	99.75	100.57	100.60
Traces (µg/g)	PSIII A7	PSIII A4.2	PSIII A2.2	PSIII A2.1	PSI 10.1	PSIII A2.0	PSIII A1.1	PSI 11.2	PSIII 12.0	PSIII 13.2	PSIII 13.4	PSIII 14.0	PSIII 15.2	PSIII 16.0	SY551	SY552
Rb	22	0	0	0	1	0	0	1	0	1	0	1	0	0		
Ba	86	20	8	20	29	22	9	20	8	7	0	2	1	7		
Sr	205	390	427	491	298	492	5	69	0	5	2	4	0	7		
Nb	3	1	1	1	2	3	6	4	5	7	4	3	2	7		
Zr	98	45	101	122	123	88	106	84	161	137	109	108	6	6		
Hf	3	2	3	3	3	3	3	3	4	4	4	4	1	1		
Y	36	32	28	30	57	38	87	45	60	12	4	0	2	0		
Ga	19	23	19	17	11	21	15	16	14	0	14	7	5	0		
Zn	75	94	75	61	51	71	129	126	97	75	55	49	99	48		
Cu	61	130	42	42	53	31	28	40	38	24	22	14	31	15		
Ni	11	18	20	32	120	45	47	42	194	167	194	658	2270	2319	2430	2577
Co	28	35	26	20	28	37	81	74	57	58	79	111	129	111		
Cr	12	22	49	54	245	46	114	43	346	276	253	222	5208	2999	2449	2706
V	360	486	422	452	257	469	371	639	225	183	128	111	48	49		
Sc	33	40	36	34	33	64	29	32	36	26	21	14	5	8		
La	2	0	4	6	0	6	17	11	25	0	0	0	0	0		
Ce	33	23	28	23	0	24	54	22	86	0	4	0	0	0		
Nd	15	12	13	11	3	12	24	12	38	6	2	51	0	0		
Pb	5	9	8	11	10	10	2	6	0	1	0	1	2	7		
Th	4	0	3	6	0	3	4	3	1	0	2	0	0	0		
U	0	0	0	0	1	0	0	0	0	0	0	0	0	0		
δ26Mg	0.13		0.06	0.16	0.20	0.23	0.20	0.33	0.53	0.49	0.50	0.02	0.01	0.02	0.09	0.11
δ25Mg	-0.23		0.15	-0.32	-0.37	-0.44	-0.39	-0.64	-1.03	-0.93	-0.97	0.01	0.00	-0.05	-0.18	-0.24
2sd	0.02		0.10	0.02	0.08	0.07	0.04	0.04	0.05	0.05	0.07	0.06	0.04	0.07		
δ26Mg rpt			-0.07	-0.17			-0.18		-0.54		-0.45		0.01			
δ25Mg rpt			-0.13	-0.35			-0.35		-1.08		-0.89		0.03			
2sd rpt			0.06	0.05			0.04		0.04		0.04		0.09			
δ18O WR	5.38	5.21	5.21	4.43	4.40	4.57		4.69	5.17	5.05	5.05	4.97	5.91	6.02	5.57	5.52
δ18O fluid	4.55	4.61	4.61	3.92	3.76	3.77		3.22	3.98	3.86	3.76	3.70	4.51	4.68	4.23	4.11

Table 2. Whole-rock major and trace element concentrations and isotope ratios of the

2

investigated samples. Repeats are full chemical repeats, including dissolution. The external reproducibility (2sd) on δ^{26}Mg of the analyses is ± 0.06‰.

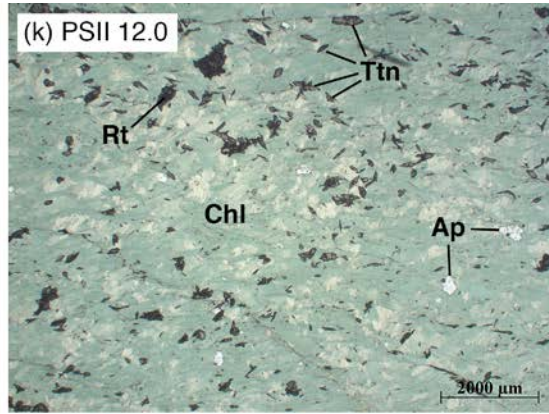|	Distance from contact (cm)	δ^{25}Mg (‰)	2sd	δ^{26}Mg (‰)	2sd
A2.1 (Zone III)	-28.5				
Omp		-0.15	0.06	-0.29	0.07
rpt		-0.16	0.05	-0.30	0.05
Chl		-0.20	0.05	-0.38	0.04
rpt		-0.16	0.03	-0.31	0.05
Gln		-0.28	0.05	-0.55	0.04
rpt		-0.32	0.03	-0.62	0.02
A2.2 (Zone II)	-31.2				
Omp		-0.09	0.03	-0.20	0.02
rpt		-0.11	0.04	-0.24	0.04
Chl		-0.15	0.03	-0.28	0.02
rpt		-0.15	0.03	-0.32	0.02
Gln		-0.10	0.03	-0.17	0.01
rpt		-0.12	0.06	-0.24	0.05
Tur		-0.03	0.05	-0.06	0.03
A4.1 (Zone II)	-36.6				
Chl		-0.16	0.02	-0.30	0.02
rpt		-0.14	0.05	-0.26	0.03
Gln		-0.17	0.05	-0.30	0.03
rpt		-0.11	0.03	-0.23	0.01
Tur		-0.01	0.04	-0.04	0.04
A7 (Zone I)	-69.3				
Gln		-0.17	0.03	-0.30	0.06
rpt		-0.15	0.04	-0.30	0.10
Chl		-0.12	0.02	-0.24	0.03
Phe		-0.24	0.04	-0.46	0.03
Grt		-0.90	0.01	-1.72	0.01
rpt		-0.83	0.01	-1.61	0.01

Table 3. Mg isotope ratios of mineral separates.
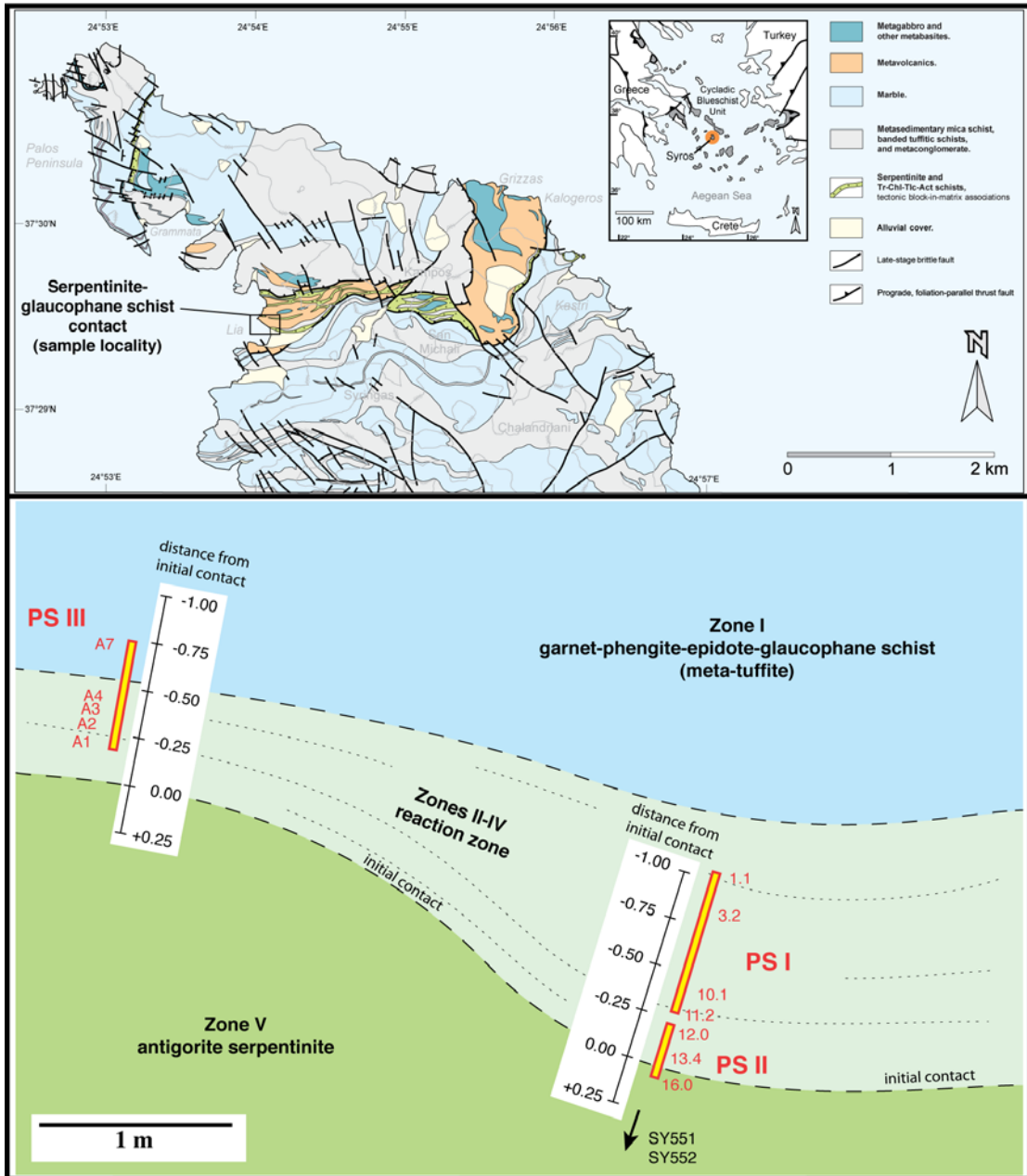
Figure 1

Figure 2

Figure 3

(a) PSIII A7.1 — Rt, Ph, Ep, Ilm, Grt, Chl, Gln, 2000 μm

(b) PSIII A6.1 — Chl, Grt, Ep, Ph, Gln, 2000 μm

(c) PSIII A5.1 — Ep, Grt, Ph, Chl, Gln, 2000 μm

(d) PSIII A4.1 — Ttn, Chl, Ph, Gln, Ep, 2000 μm

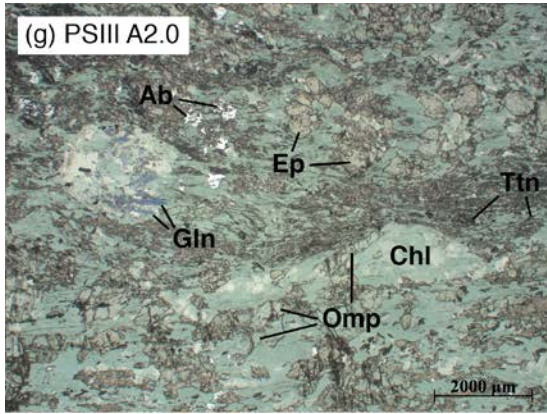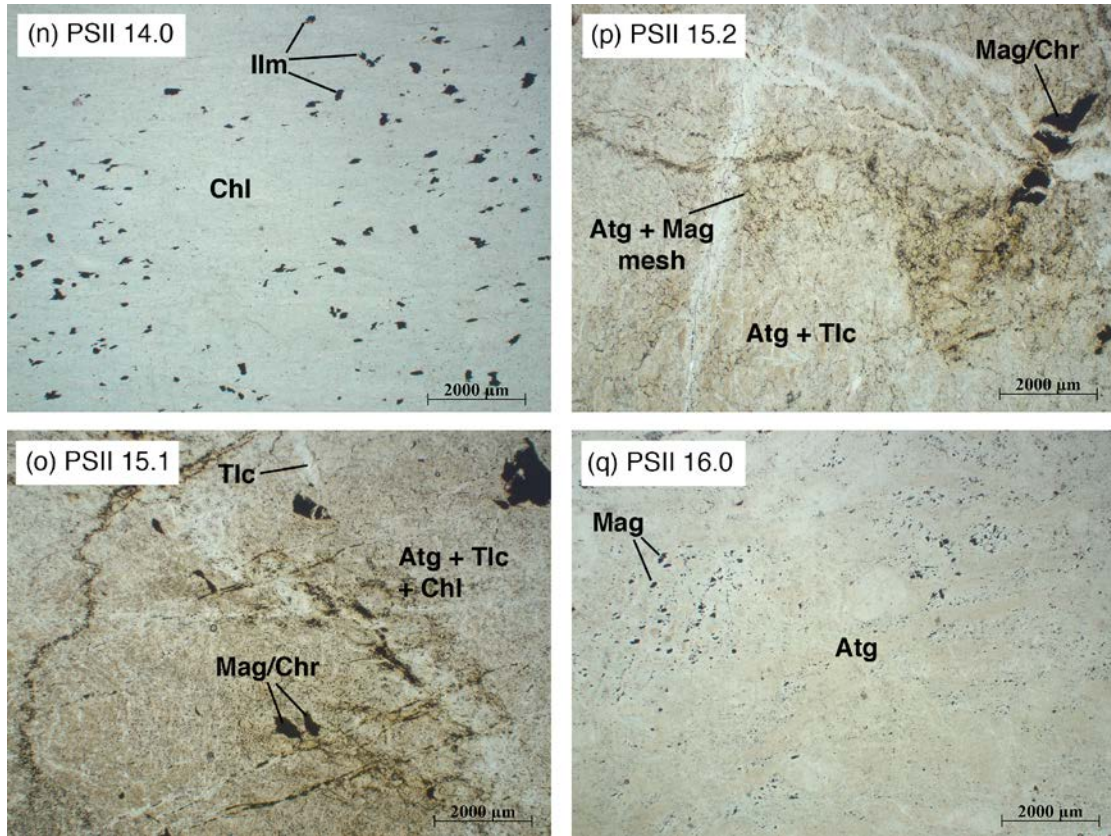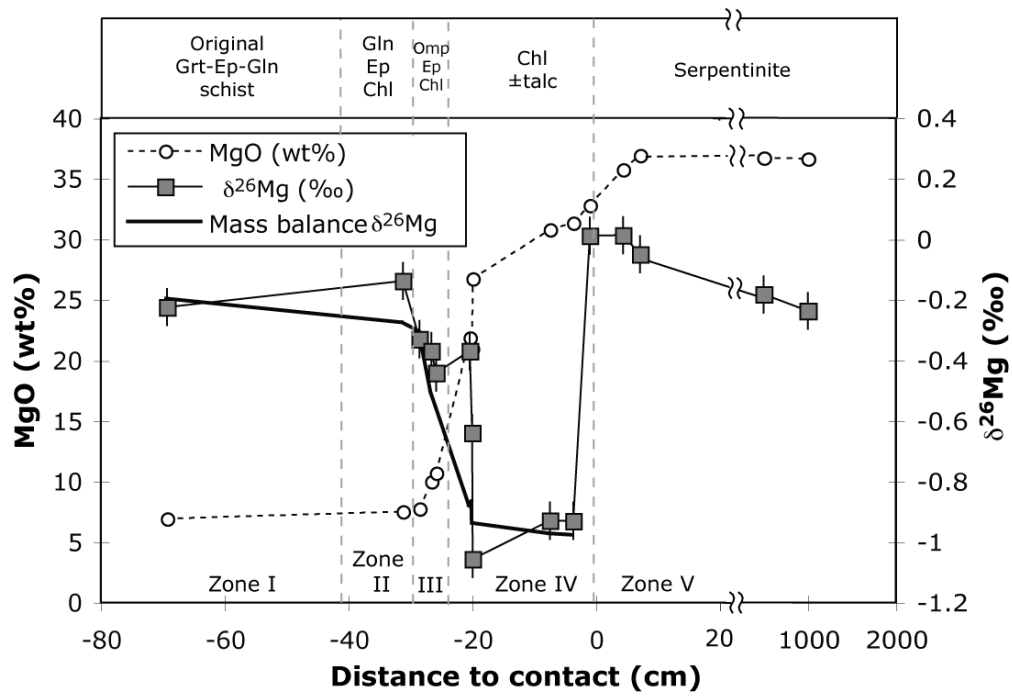(e) PSIII A2.1 — Chl, Ep, Ab, Omp, Gln, 2000 μm
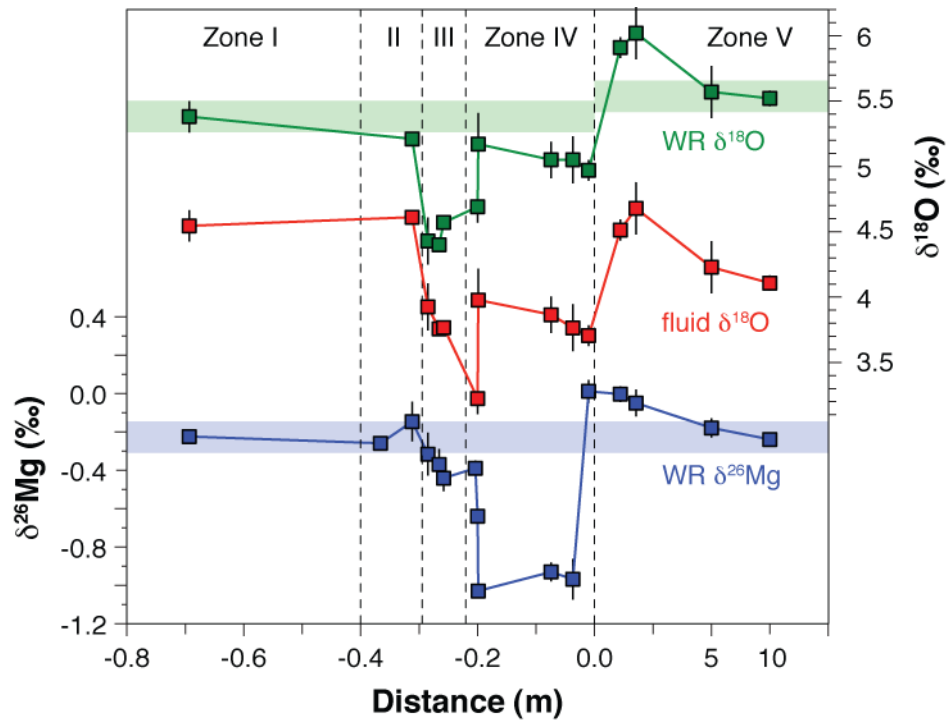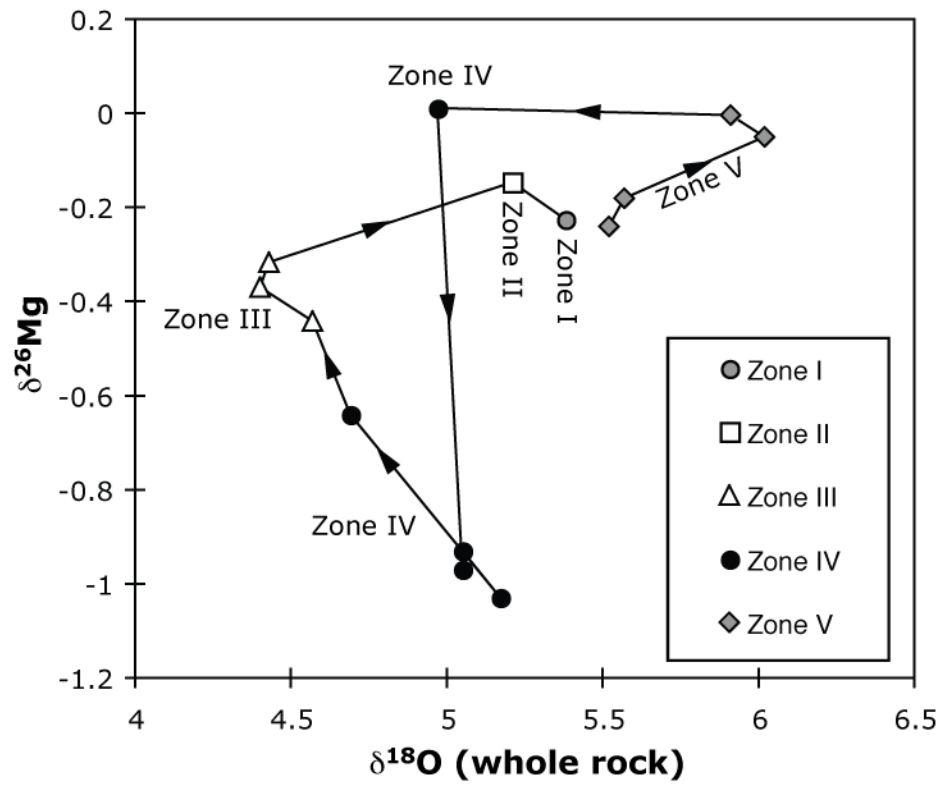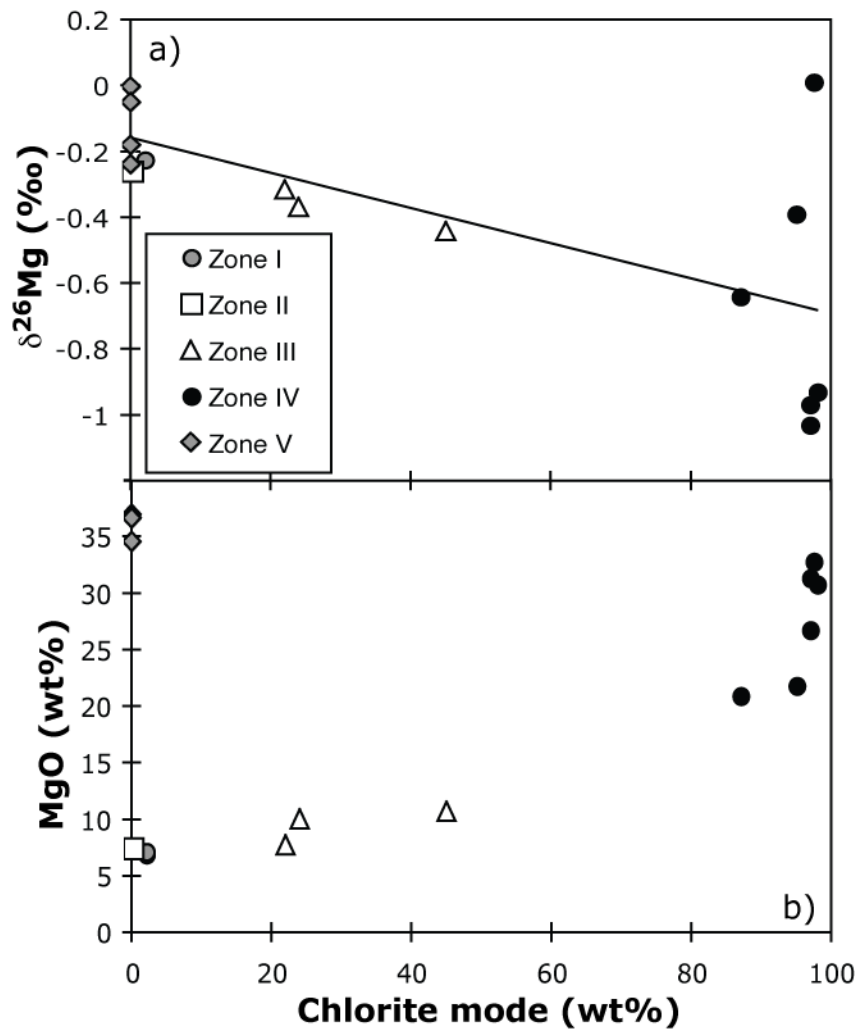
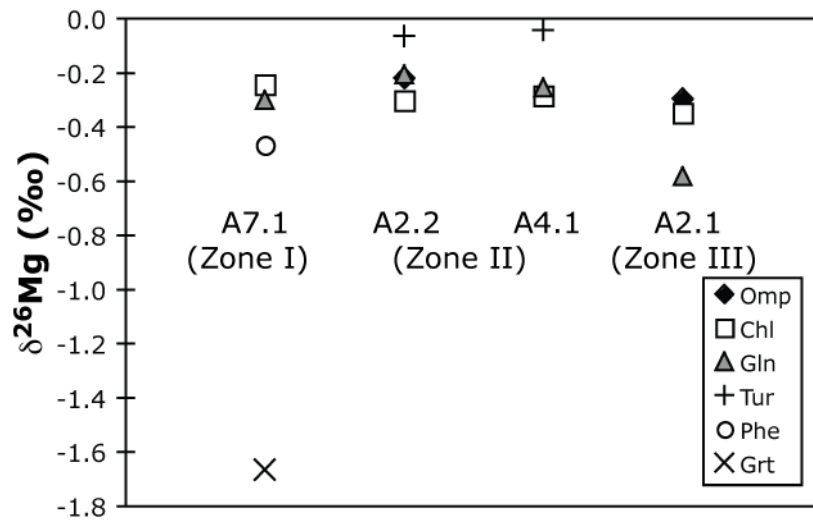(f) PSI 10.1 — Ep, Ttn, Omp, Ab, Chl, 2000 μm
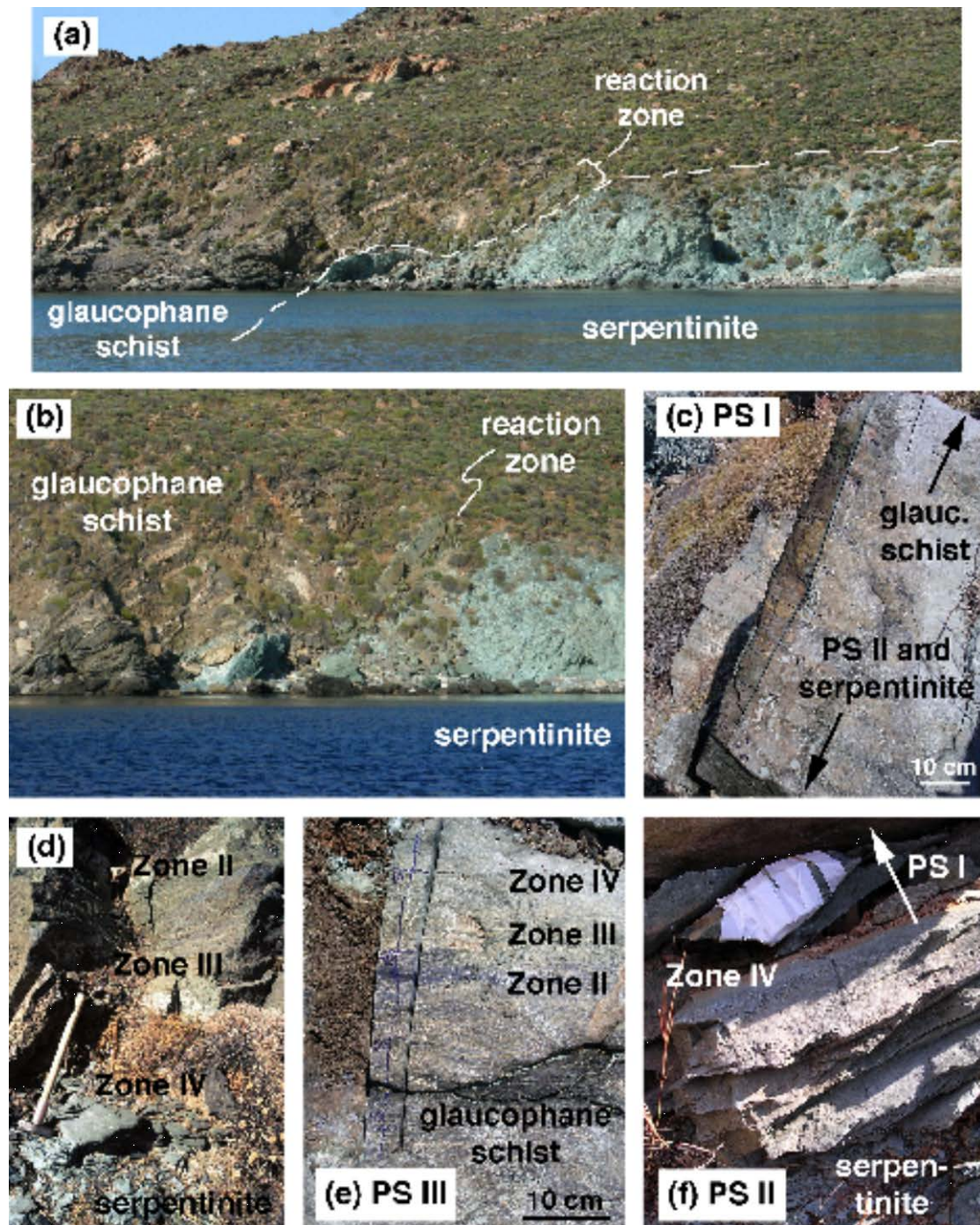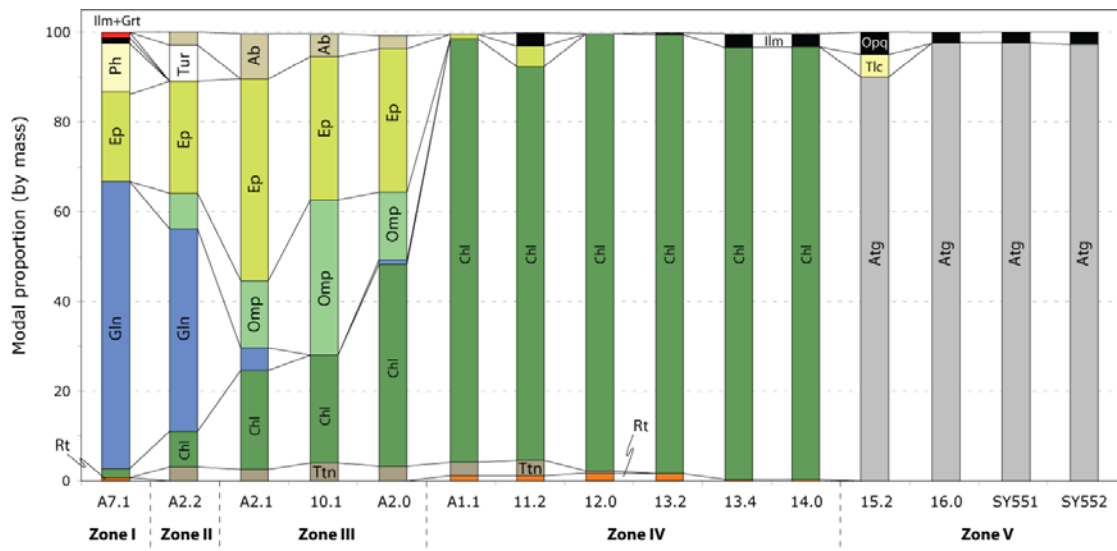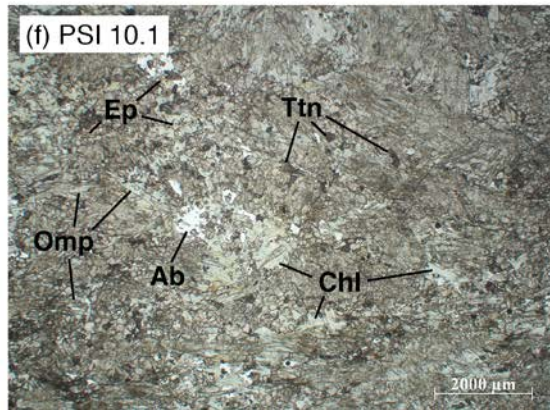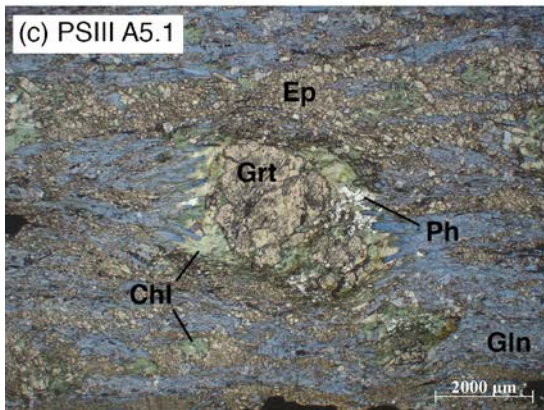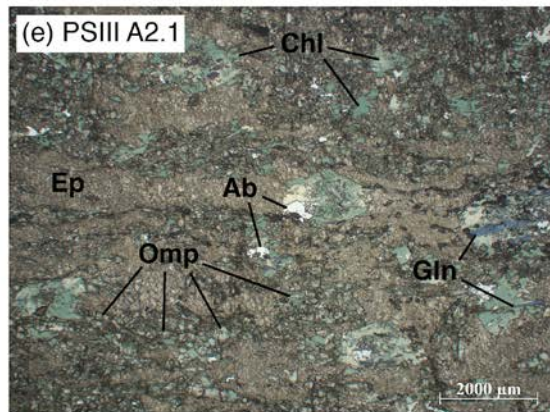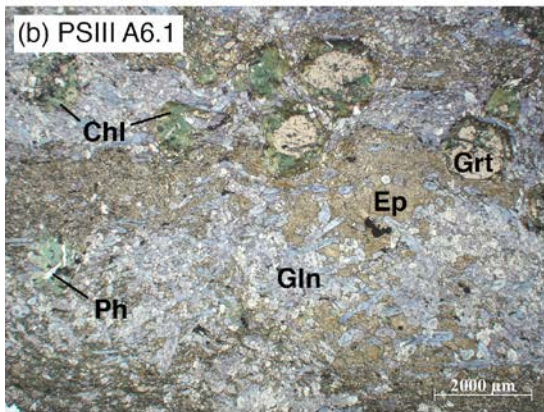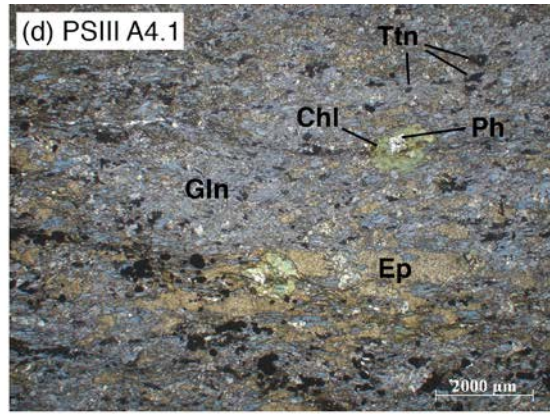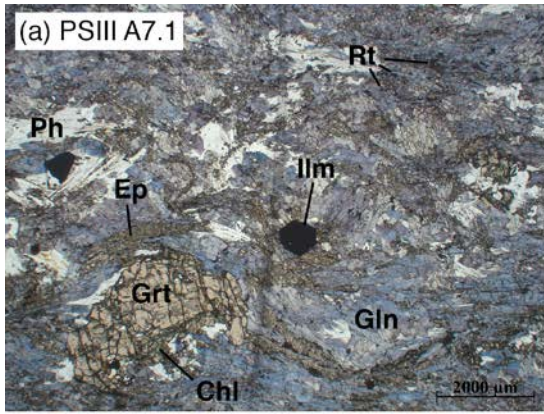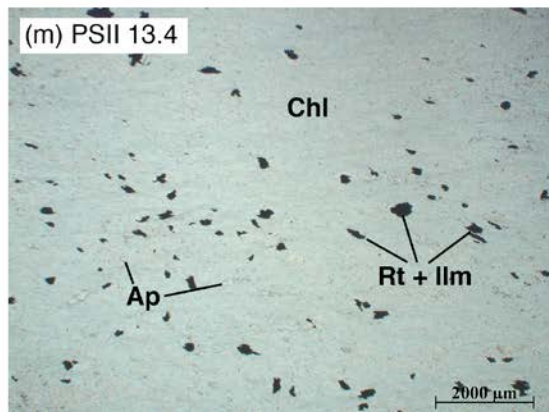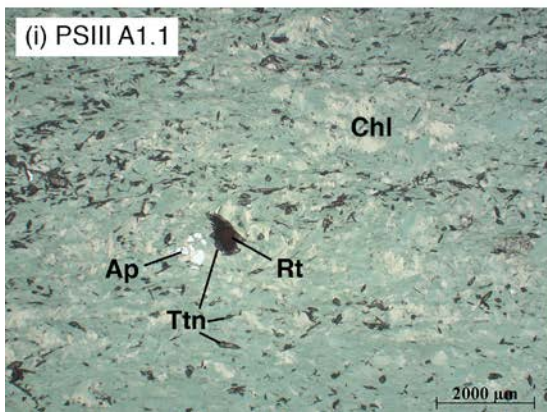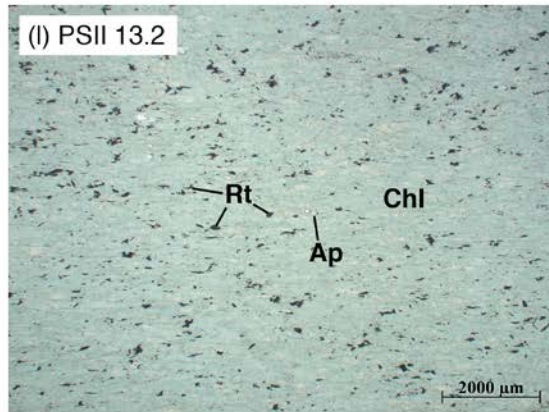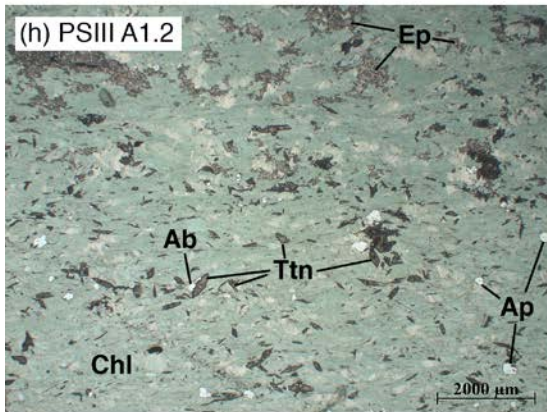
Figure 4

Figure 5

Figure 6

Figure 7

Figure 8

Figure 9
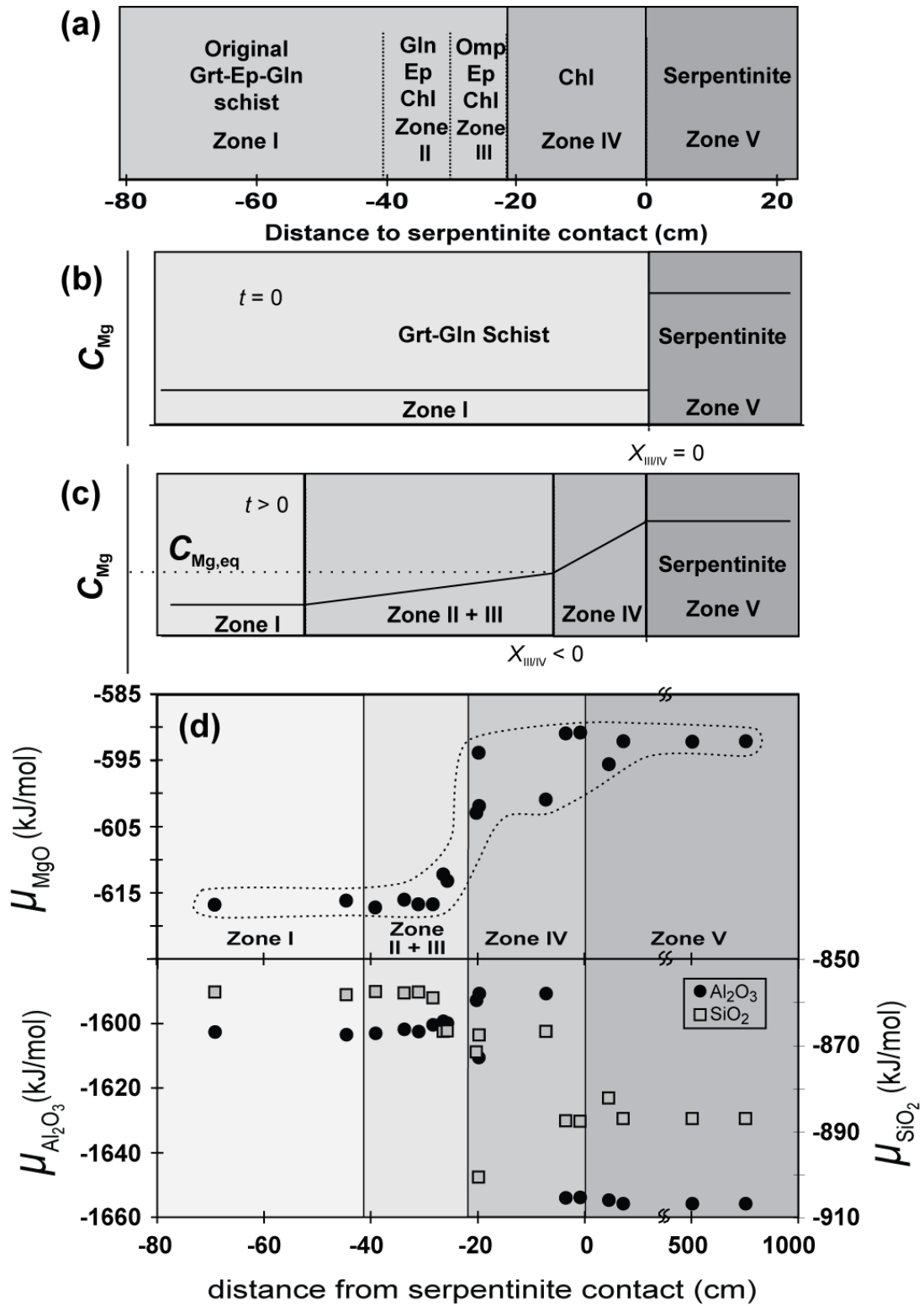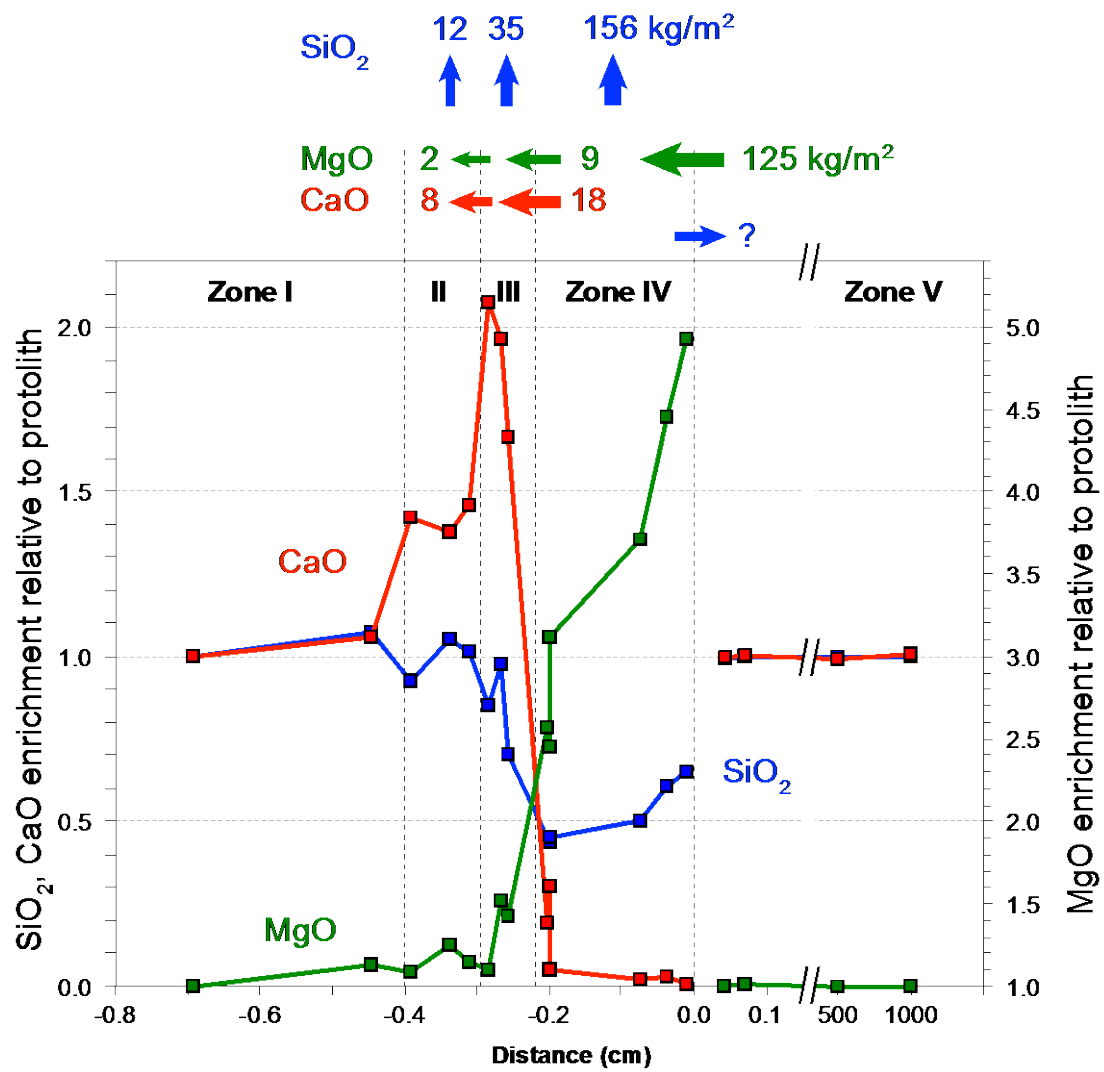
Figure 10

Figure 11

(a) k_{IV} = 1.7e-10 cm^2/s
D_{Mg} = 1.e-5 cm^2/s
β = 0.05
Θ = 1.e-3

Initial
18 kyr
24 kyr
42 kyr
54 kyr

(c) k_{IV} = 1.03e-10 cm^2/s
D_{Mg} = 1.e-5 cm^2/s
β = 0.05
Θ = 1.e-3

Initial
10 kyr
30 kyr
50 kyr
100 kyr

(e) k_{IV} = 2.05e-11 cm^2/s
D_{Mg} = 1.e-5 cm^2/s
β = 0.05
Θ = 1.e-3

Initial
50 kyr
200 kyr
350 kyr
500 kyr

(g) k_{IV} = 6.37e-12 cm^2/s
D_{Mg} = 1.e-5 cm^2/s
β = 0.05
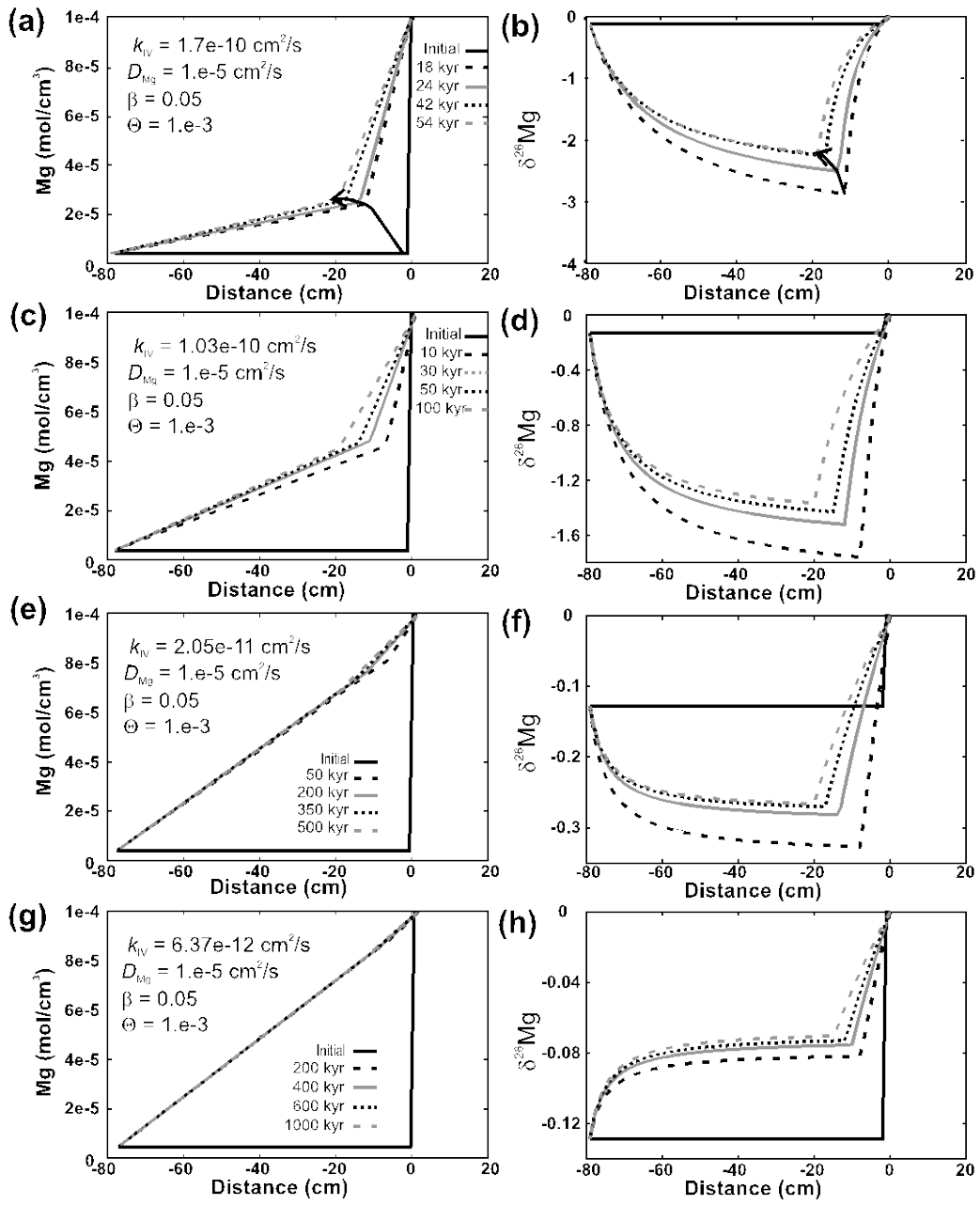Θ = 1.e-3
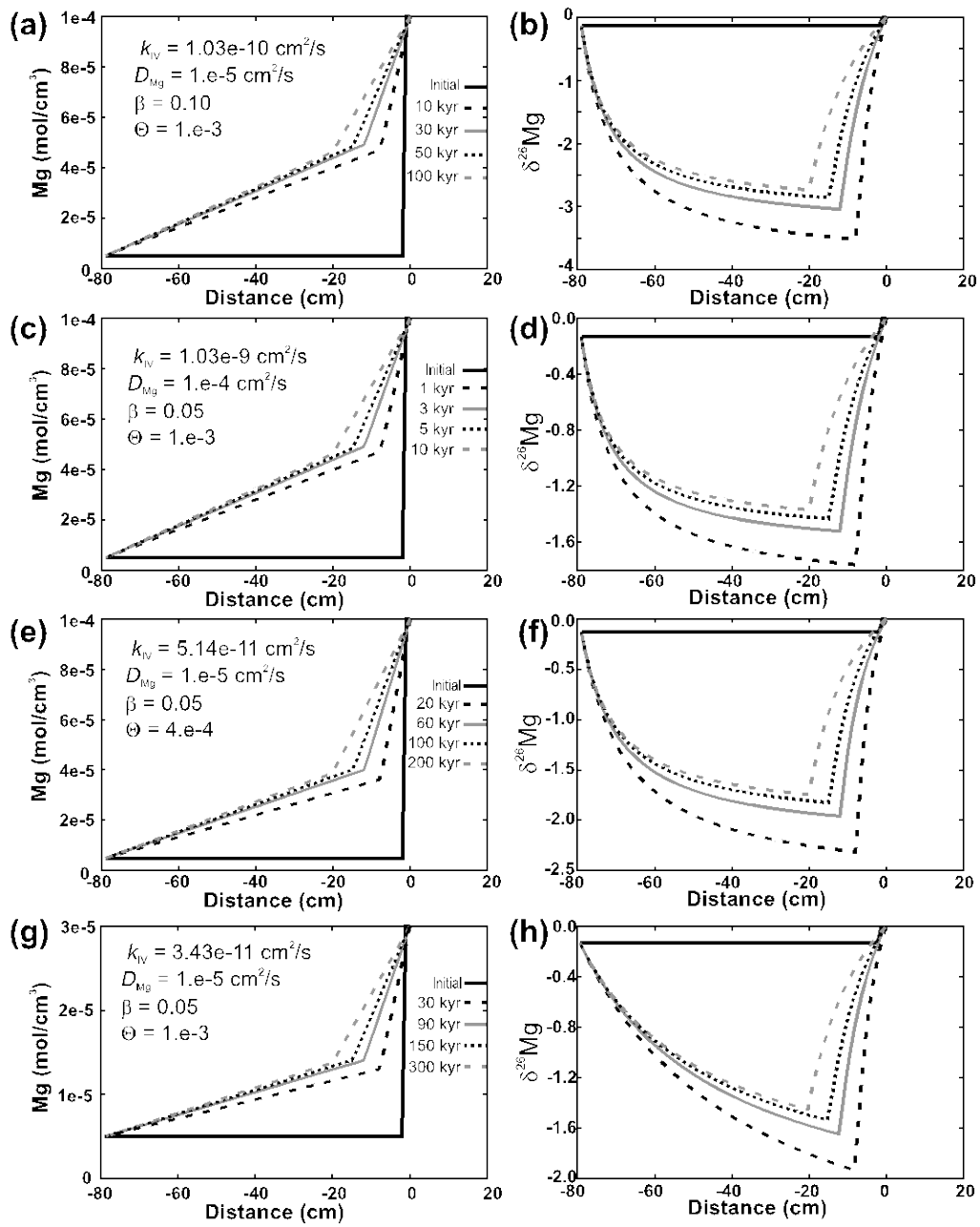
Initial
200 kyr
400 kyr
600 kyr
1000 kyr

Figure 12

Figure 13

Appendix

Numerical solution method of the diffusion reaction model

We used a finite difference scheme to numerically solve the moving boundary problem governed by Equations 9-11. The *x-t* space is separated into a grid with equidistant steps δx and δt. The concentration at each grid point is denoted by $C_{n,m}$ where n and m represent the respective coordinates of the grid point and hence $C_{n,m}$ is the concentration of the isotope at position $n \cdot \delta x$ at time $m \cdot \delta t$. The moving boundary was considered by using a front tracking method as described in Crank (1975). The interface of zone III/IV is changing continuously during the evolution of the reaction zone but the grid system in the finite difference model is fixed with a set of equidistant grid points as illustrated in Fig. A1. To consider the variable position of the interface in the model, a new variable p_j is introduced, which is simply defined as the fractional distance between the position of the boundary and the grid point i behind this moving boundary at time $j \cdot \delta t$ (Fig. A1). Consequently, the value of p_j is given by:

$$p_j = \frac{X_{\text{III/IV}}(t) - i \cdot \partial x}{\partial x} \qquad (A1)$$

where $X_{\text{III/IV}}(t)$ is given by a parabolic rate law with growth constant k (see main text). Using the Langrangian type interpolation formulae it can be shown that for the grid point i with $i \cdot \delta x < X_{\text{III/IV}}(t)$ and $(i+1) \cdot \delta x > X_{\text{III/IV}}(t)$ the following numerical approximations for the first and the second derivative of the concentration after the distance variable x can be derived (Crank 1975):

$$\left. \frac{\partial^2 C}{\partial x^2} \right|_{x=i\partial x} = \frac{2}{\partial x^2} \cdot \left(\frac{C_{i-1,j}}{p_j+1} - \frac{C_{i,j}}{p_j} + \frac{C_{B,j}}{p_j \cdot (p_j+1)} \right) \qquad (A2)$$

$$\left.\frac{\partial C}{\partial x}\right|_{x=X^{IV}_{III/IV}} = \frac{1}{\partial x}\cdot\left(\frac{p_j\cdot C_{i-1,j}}{p_j+1} - \frac{(p_j+1)\cdot C_{i,j}}{p_j} + \frac{(2p_j+1)\cdot C_{B,j}}{p_j\cdot(p_j+1)}\right) \qquad (A3)$$

$$\left.\frac{\partial^2 C}{\partial x^2}\right|_{x=(i+1)\partial x} = \frac{2}{\partial x^2}\cdot\left(\frac{C_{B,j}}{(1-p_j)(2-p_j)} - \frac{C_{i+1,j}}{1-p_j} + \frac{C_{i+2,j}}{2-p_j}\right) \qquad (A4)$$

$$\left.\frac{\partial C}{\partial x}\right|_{x=X^{III}_{III/IV}} = \frac{1}{\partial x}\cdot\left(\frac{(2p_j-3)\cdot C_{B,j}}{(1-p_j)(2-p_j)} + \frac{(2-p_j)\cdot C_{i+1,j}}{1-p_j} - \frac{(1-p_j)\cdot C_{i+2,j}}{2-p_j}\right) \qquad (A5)$$

$C_{B,j}$ is the concentration at the moving boundary at time $j\cdot\delta t$. We applied the explicit finite difference scheme (Crank 1975) and thus with Equations A1-A5 the set of governing equations can be expressed, as follows:

For $n < i$ and $n > i +1$:

$$C_{n,j+1} = C_{n,j} + \frac{D\cdot\partial t}{\partial x^2}\cdot\left(C_{n-1,j} - 2C_{n,j} + C_{n+1,j}\right) \qquad (A6)$$

For $n = i$ and $n = i + 1$

$$C_{i,j+1} = C_{i,j} + \frac{2D\cdot\partial t}{\partial x^2}\cdot\left(\frac{C_{i-1,j}}{p_j+1} - \frac{C_{i,j}}{p_j} + \frac{C_{B,j}}{p_j\cdot(p_j+1)}\right) \qquad (A7)$$

$$C_{i+1,j+1} = C_{i+1,j} + \frac{2D\cdot\partial t}{\partial x^2}\cdot\left(\frac{C_{B,j}}{(1-p_j)(2-p_j)} - \frac{C_{i+1,j}}{1-p_j} + \frac{C_{i+2,j}}{2-p_j}\right) \qquad (A8)$$

The boundary condition at $x = X_{III/IV}(t)$ (Eqns. 9 and 11) can be expressed as:

$$-\frac{D\cdot\Theta}{\partial x}\cdot\left(\frac{p_j\cdot C_{i-1,j}}{p_j+1} - \frac{(p_j+1)\cdot C_{i,j}}{p_j} + \frac{(2p_j+1)\cdot C_{B,j}}{p_j\cdot(p_j+1)}\right) =$$

$$\frac{dX_{III/IV}}{dt}\left(C^{IV}_{Mg} - C^{III}_{Mg}\right) - \frac{D\cdot\Theta}{\partial x}\cdot\left(\frac{(2p_j-3)\cdot C_{B,j}}{(1-p_j)(2-p_j)} + \frac{(2-p_j)\cdot C_{i+1,j}}{1-p_j} - \frac{(1-p_j)\cdot C_{i+2,j}}{2-p_j}\right)$$

$$(A9)$$

Equation A9 can be used to calculate $C_{B,j}$ after each time step:

$$C_{B,j} = \dfrac{\dfrac{p_j \cdot C_{i-1,j}}{p_j+1} - \dfrac{(p_j+1)\cdot C_{i,j}}{p_j} - \dfrac{(2-p_j)\cdot C_{i+1,j}}{1-p_j} + \dfrac{(1-p_j)\cdot C_{i+2,j}}{2-p_j} + \dfrac{v_{III/IV}\left(C_{Mg}^{IV} - C_{Mg}^{III}\right)\partial x}{D\Theta}}{\dfrac{-(2p_j+1)}{p_j\cdot(p_j+1)} + \dfrac{(2p_j-3)}{(1-p_j)(2-p_j)}}$$

(A10)

For the simulation a C++ program was written, where the following iterative

procedure was applied to each of the Mg isotopes:

(i)   Initialization of the concentration distribution for $j = 0$, which defines the

values $C_{n,0}$ (see Fig. 8b).

(ii)   Set $j = j+1$ and calculate p_j from Eqn. A1 and $C_{B,j}$ from Eqn. A10.

(iii)   Calculate $C_{n,j+1}$ from for $n = (1,…,N-1)$ with Equations A6-A8. The values

of $C_{0,j+1}$ and $C_{N,j+1}$ are defined by the initial value due to the fixed

boundary condition (meaning infinite reservoirs at the two ends of the

model system)

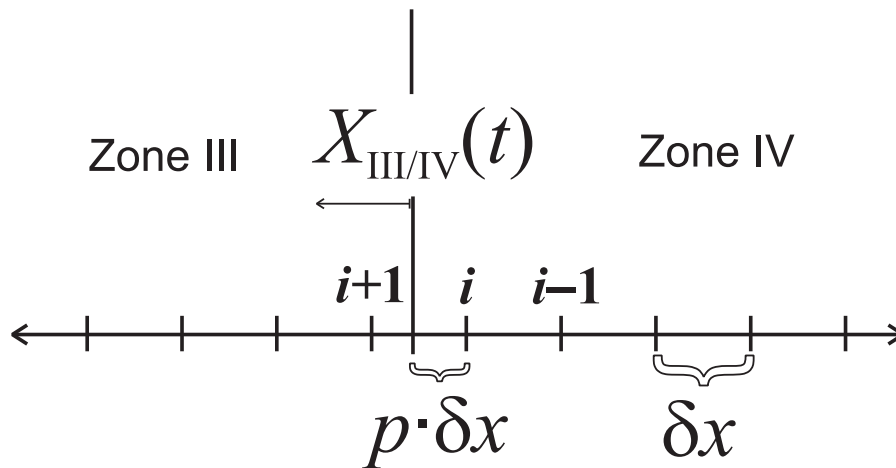(iv)   Start again with step (ii) until $j\delta t$ = total time.

Figure A1.